THESIS FOR THE DEGREE OF DOCTOR OF PHILOSOPHY IN MACHINE AND VEHICLE SYSTEMS

Optimizing torque distribution for enhanced energy efficiency in battery electric vehicles

JULIETTE TORINSSON

Department of Mechanics and Maritime Sciences

CHALMERS UNIVERSITY OF TECHNOLOGY

Göteborg, Sweden 2025

Optimizing torque distribution for enhanced energy efficiency in battery electric vehicles
JULIETTE TORINSSON
ISBN 978-91-8103-290-1

Doktorsavhandlingar vid Chalmers tekniska högskola
Ny serie nr. 5748
ISSN 0346-718X
Department of Mechanics and Maritime Sciences
Chalmers University of Technology
SE-412 96 Göteborg
Sweden
Telephone: +46 (0)31-772 1000

Chalmers Digitaltryck
Göteborg, Sweden 2025

Optimizing torque distribution for enhanced energy efficiency in battery electric vehicles
JULIETTE TORINSSON
Department of Mechanics and Maritime Sciences
Chalmers University of Technology

Abstract

This thesis addresses the energy management problem (EMP) in battery electric vehicles (BEVs), focusing on the optimization of velocity trajectory and torque distribution in vehicles equipped with multiple electric motors. Optimization-based control allocation is a widely used method for coordinating motor redundancy to enhance energy efficiency. It is based on the simplifying assumption that vehicle motion control and actuator coordination can be addressed independently. In other words, it assumes that the two subproblems constituting the EMP, i.e., finding the energy-optimal velocity trajectory and torque distribution, can be solved *sequentially*, as opposed to *simultaneously*. However, it is found in this thesis that the two subproblems are inherently coupled, as the optimal velocity trajectory depends on the efficient regions of the motors. The first part of this thesis investigates the energy consequences of solving the EMP sequentially versus jointly in a BEV with two electric motors, one per axle. Two optimization architectures are evaluated: a centralized architecture (CA) and de-centralized architecture (DCA). CA jointly optimizes the velocity trajectory and torque distribution for minimal energy consumption in a predictive framework, while DCA solves these subproblems hierarchically: velocity trajectory optimization is performed predictively, and torque distribution is computed instantaneously. This decoupling leads to an increase in energy consumption of 3.5% at low velocities, 2.2% in an urban city cycle, and up to 8.2% at high peak road grades compared to CA. To mitigate the energy consequences, the objective function in the predictive layer of DCA is augmented with an aggregated power loss map (APLM), which achieves energy savings close to CA. The second part of the thesis explores torque allocation strategies in a BEV with four identical permanent magnet synchronous motors (PMSMs) to minimize motor and tire power losses during moderate driving. Due to the significant idle losses of PMSMs, mechanical decoupling is crucial and identified as the main source of energy savings. A quadratic programming (QP) algorithm is developed to optimize torque distribution and manage couplings, reducing energy consumption by 3.9% compared to equal torque distribution; without couplings, the reduction drops to 0.2%. Tire losses, including lateral slip losses during cornering, are found to have minimal impact on energy consumption compared to motor losses during moderate driving. In addition, the single-speed transmission ratios of the front and rear motors are optimized for minimal energy consumption, alongside torque distribution. When coordinated optimally, the optimal ratios result in one axle configured for low-speed and the other for high-speed efficiency. This leads to a reduction in energy consumption by 8.4% compared to a setup with equal torque distribution and equal transmission ratios. In summary, during moderate driving, knowledge of motor losses is found to be the most significant contributor to reducing energy consumption in BEVs by optimizing the speed profile and torque distribution.

Keywords: electric vehicle, optimization, energy efficiency, torque distribution, speed planning, eco-driving

To my boys:
Daniel, Gustav & Emil.

"Ka-chow!"

- Lightning McQueen

Acknowledgements

I have been on this PhD journey for a long time. There are so many people I am grateful for who have supported me along the way. I am extremely lucky to have been guided by an excellent supervision team, not only supporting me in my work, but also caring earnestly about my well-being. First of all, I would like to thank my main supervisor, Associate Prof. Mats Jonasson. Your deep knowledge within both research and industry, your undying and contagious curiosity, and never-ending support has not only contributed significantly to my growth as a researcher, but also helped me to endure and complete my dissertation. I will miss working with you, and I hope there will be more projects for us in the future. I would also like to thank my industrial supervisor, Dr. Derong Yang, for her positive spirits and excellent competence in anchoring the research in possible industrial solutions. I look forward to continue working with you. Thank you, Prof. Bengt Jacobson, for always providing an alternative view to everything with playfulness, not only expanding my knowledge but aiding me in clarifying my thoughts.

I am grateful to my colleagues at Volvo Cars, particularly Niklas Karlsson and Mikael Ågren, for always inviting me for lunch when I am in Torslanda, and for our rejuvenating lunch walks. I want to express special thanks to my manager, Anna Söderlund, for your endless support and understanding of the PhD journey. I truly would not have been able to finish without your encouragement. I would also like to acknowledge the financial support of Energimyndigheten, without which this project would not have been possible.

I want to thank past and present colleagues and friends at VEAS: Sina, Randi, Magnus, Johannes, Anandh, Erik, Krister, Björnborg, Ektor, and many more. You have made the working environment so enjoyable, with many interesting discussions and lots of laughter. Thank you, Simone, for managing such an excellent division. A special thanks to Sonja, the hero of PhD students, and the heart of VEAS.

To my family and old friends. Mamma, thank you for teaching me that the sky is the limit. Your magical ability to solve every problem, no matter the complexity, is beyond me. I am to consider myself lucky to have inherited a fraction of that skill. Hanna, systrami, and Emma, thank you for being there for me in every way, making me feel so loved and seen. One could not wish for better friends.

Finally, min älskade Daniel, words cannot express the magnitude of your significance during this journey that started seven years ago. Life is completely different now, with our beloved two boys, and time for recovery is limited. Yet, somehow, you have managed not only to run our household and feed the entire family during the creation of this thesis, but also to remain a calm, loving, and generous partner. You have selflessly given me the space I've needed while I've increasingly drifted away mentally, especially towards the end. Your contribution to this thesis is equal to mine.

Juliette Torinsson
Göteborg, May 2025

Nomenclature

Abbreviations

ABS	Anti-lock braking system
APLM	Aggregated power loss map
ASM	Asynchronous motor
AUC	Artemis urban cycle
AWD	All wheel drive
BEV	Battery electric vehicle
CA	Centralized optimization architecture
DCA	De-centralized optimization architecture
DP	Dynamic programming
ED	Equal distribution
EFU	Equal friction utilization
EMP	Energy management problem
ESC	Electronic stability control
FWD	Front wheel drive
GCC	Gothenburg city cycle
HEV	Hybrid electric vehicle
ICE	Internal combustion engine
LUT	Lookup table
MPC	Model predictive control
OCP	Optimal control problem
PMSM	Permanent magnet synchronous motor
PnG	Pulse and glide
QP	Quadratic program
r-DCA	Refined de-centralized optimization architecture
RWD	Rear wheel drive
SOC	State of charge
TC	Traction control

Thesis

This thesis consists of an extended summary of the following appended papers:

Paper A Torinsson, J., Jonasson, M., Yang, D., and Jacobson, B. "Energy reduction by power loss minimisation through wheel torque allocation in electric vehicles: a simulation-based approach". *Vehicle System Dynamics* **60**.5 (2020), 1488–1511. DOI: 10.1080/00423114.2020.1858121

Paper B Torinsson, J., Jonasson, M., Jacobson, B., and Yang, D. "Joint Optimization of Transmission and a Control Allocator to Minimize Power Losses in Electric Vehicles". *Advances in Dynamics of Vehicles on Roads and Tracks II. IAVSD 2021* (2021). DOI: 10.1007/978-3-031-07305-2_106

Paper C Torinsson, J., Jonasson, M., Yang, D., and Jacobson, B. "Upper bounds of lateral tire slip loss minimization during daily driving using torque vectoring". *AVEC'22. 15th International Symposium on Advanced Vehicle Control* (2022)

Paper D Torinsson, J., Jonasson, M., Yang, D., Jacobson, B., and Ghandriz, T. "Energy consequences of separating velocity planning and torque distribution in overactuated electric vehicles". *submitted to Transportation Engineering* (2025)

The author of the thesis was responsible for the modeling, simulation and analysis. The co-authors contributed with valuable discussions. The power loss data of the motors and transmission were provided by Volvo Cars. The papers were initially written by Torinsson, and then discussed, reviewed and revised by all authors.

Patent grants by the author:

1. Utbult[1], J., Jonasson, M., Yang, D., and Jacobson, B., "Method and system to control torque distribution", Patent No. 11738739, 2023.
2. Torinsson, J., Yang, D., Jonasson, M., and Jacobson, B., "Method to decrease power consumption of steering actuator by torque vectoring", Patent No. 12351039, 2025.

Patent applications by the author:

1. Torinsson, J. and Jonasson, M., "Management of torque distribution in an electric vehicle based on power loss maximization and minimization", European patent application no. 24206282.6, 2024.

[1] Author's previous surname.

2. Torinsson, J., Jonasson, M., and Yang, D., "Energy efficient speed recommendation based on lumped powertrain efficiency for electric vehicles", European patent application no. 24180622.3, 2024.

Contents

Part I

Extended summary

1

Introduction

The urgency to reduce emissions has never been greater than it is today. Unprecedented changes in every sector are necessary to keep the global temperature increase within the limits set by the Paris Agreement. In 2019, road transport accounted for 25% of the European Union's greenhouse gas emissions with car transport contributing 43.9% [1]. It is recognized that a significant uptake of electric vehicles is needed. Governmental subsidies and tax incentives are associated with the ownership of battery electric vehicles (BEVs), which accounted for 15% of new car registrations in 2023 [2]. Even though the number has been growing rapidly since 2019, lower driving range and long charging times are some among several factors affecting public acceptance negatively [3], ultimately limiting market penetration. Consequently, energy management strategies for BEVs are widely researched.

1.1 Background

In a transport mission, a certain amount of energy is inevitably required to overcome factors such as road grade and air drag. However, the total energy consumption of the vehicle is higher due to additional losses within the drivetrain and friction brakes. The driving style significantly influences energy use, where aggressive driving characterized by harsh acceleration and deceleration increases consumption [4, 5], mainly due to losses related to frequent changes in kinetic energy. Drivers have been encouraged to adopt eco-driving, i.e., an energy-efficient driving style, to reduce the energy consumption. However, increased connectivity and autonomy of vehicles allow for algorithms to preview upcoming road segments and plan motion accordingly in an energy-efficient manner. These algorithms can then be employed in the vehicle to assist the driver to more energy-efficient driving, such as Mercedes' function Eco-Assist [6], which evaluates information on route, speed limits and topography, prompts the driver to take the foot off the accelerator pedal, and then decelerates the vehicle accordingly by adaptive regenerative braking. Drivers of heavy vehicles are further aided by energy efficient cruise controllers, such as Volvo Trucks' I-See [7] and Scania's CCAP (cruise control with active prediction) [8] which utilizes information on upcoming terrain to adapt speed and gear-shifting to minimize fuel consumption.

Further opportunities to reduce energy consumption emerge with the electrification of vehicles and the integration of multiple actuators within the powertrain. Previously, there was only one actuator to generate the forward motion in a conventional vehicle - the internal combustion engine (ICE). In BEVs, the powertrain commonly consists of multiple actuators, i.e., electric motors, controlling the same degree of freedom. A vehicle with such a powertrain is *overactuated*. In this case, a longitudinal force request, corresponding to a request on forward motion, can be fulfilled by an infinite number of torque distributions between the motors. The redundancy of

motors enable the pursuit of secondary objectives, such as reducing the energy consumption, by allocating torque to minimize the power losses in the drivetrain.

The driving style and operation of the powertrain are inherently coupled, as the driving style determines the power demand that the powertrain must fulfill. In literature, these problems in BEVs are typically solved *sequentially* as opposed to *simultaneously*. The division offers benefits in terms of reduced development costs and computational effort, but might result in reduced potential to minimize energy consumption.

The energy management problem (EMP) addressed in this thesis relates to the energy-optimal velocity profile and torque distribution for BEVs with multiple electric motors. Initially, an overview of literature concerning energy-efficient torque distribution for overactuated BEVs is provided, discussing the structure of, and solution methods to, the control allocation problem. Then, the effect of single-speed transmission ratio is briefly touched upon, and how appropriate selection of the ratio in combination with deliberate torque allocation can lead to further reductions in energy consumption. Finally, the topic of energy-efficient velocity trajectories is briefly discussed, highlighting the energy-benefit of optimizing velocity trajectory jointly with powertrain operation.

1.1.1 Energy-efficient torque distribution for BEVs

Energy-efficient torque distribution for BEVs is based on the principles of control allocation. Control allocation is an approach to solve the control problem concerning overactuated systems by distributing the total control demand among several actuators [9]. The actuator selection task is separated from the regulation task in the control design, resulting in a hierarchical control architecture. In the regulation task, the total control effort to be fulfilled is specified, but not how to fulfill it. Through this separation, the choice of actuator can be optimized for the considered application. Previously, it was mainly used for marine and aerospace applications, but in recent years it has been increasingly popular for automotive applications, e.g., in yaw stability control and electric propulsion [10].

One of the first studies regarding energy-efficient torque distribution for BEVs was put forward by [11], which identified that the common method to penalize actuator effort to improve energy efficiency does not necessarily result in minimal energy consumption, as it does not consider actuator efficiencies. Instead, the objective was reformulated to penalize the instantaneous power consumption of the actuators, successfully leading to less energy consumption while fulfilling the demand on vehicle motion. This study was the spark to a large body of research that now exists on the topic [12–29]. Depending on powertrain configuration, it is predominantly the longitudinal and yaw directions of the vehicle that are overactuated. Overactuation in the longitudinal direction occurs when there is at least one motor per axle, and in the yaw direction when there are two motors on at least one axle (or one motor and a torque vectoring differential on one axle as in [23]).

Control allocation

Figure 1.1 presents a generalized overview of the control architecture found in literature for control allocation applied to electric propulsion systems. The control of couplings is not included. A high-level motion controller translates the request on vehicle motion, based on driver input

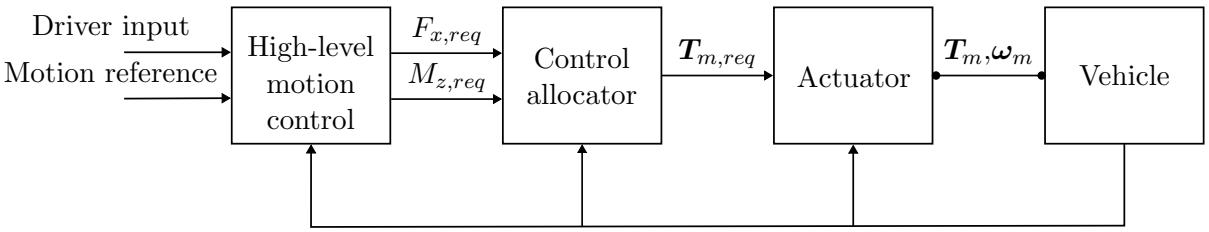

Figure 1.1: *Generalized control architecture for electric propulsion used in literature. Control of couplings not included.*

and/or motion references, to global force and moment requests to be fulfilled by the actuators. For example, interpretation of the accelerator and brake pedal position provides a longitudinal force request, and steering wheel angle in combination with a yaw rate reference provides a yaw moment request. The task of following a specific trajectory is typically not included in this architecture, as it is managed outside by, e.g., a driver or an algorithm. The control allocator receives force and moment requests and allocates corresponding required motor torques based on power efficiency, i.e, minimized power consumption. The actuator can limit torque requests exceeding the motors' operational domain or tire friction force, and/or ensure smooth ramp-up of torque to avoid drivability issues. The torque is then applied to the vehicle.

Control allocation is meant to be performed real-time, calling for computationally efficient solutions. For that purpose, non-linear dynamic systems are often linearized around a local point, e.g., the previously applied control input [9]. In the application to electric propulsion, it is common to linearize around zero angles, i.e., the small angle approximation, and only consider the effect of motor torque on longitudinal force and yaw moment by neglecting the effect of the steered wheels on longitudinal force. The optimization problem in the control allocator takes the general form,

$$\min_{\boldsymbol{u}} \quad P(\boldsymbol{u}, \boldsymbol{x}) \tag{1.1}$$

$$s.t. \quad \boldsymbol{v} = B\boldsymbol{u} \tag{1.2}$$

$$\boldsymbol{u} \in \mathbb{U} \tag{1.3}$$

where $\boldsymbol{u} \in \mathbb{R}^{m\times 1}$ represents the *true control input* usually consisting of motor torque requests $\boldsymbol{T}_{m,req}$, the set $\mathbb{U}$ includes the constraints on $\boldsymbol{u}$ defined by motor operational limits and available tire friction force, $\boldsymbol{x}$ represents the state vector, e.g., forward velocity v_x, $\boldsymbol{v} \in \mathbb{R}^{k\times 1}$ the *virtual control input* consisting of the global force and moment requests ($F_{x,req}$ and $M_{z,req}$), $P(\cdot)$ is an expression of total power or power losses to be minimized, and $B \in \mathbb{R}^{k\times m}$ is the *control effectiveness matrix* mapping the true control input to the virtual control input, e.g., the relation between motor torques and motion requests. In the case of $m = k$, i.e., B is square, the solution u^* can be found by inverting $B : u^* = B^{-1}v$, assuming B is invertible. Considering an overactuated system, B is a wide matrix $m > k$ that has rank k and is not invertible, leading to an infinite number of solutions.

Objective function

The power losses considered in literature mainly origin from the electric powertrain. The power losses in the motors are derived either from models [14], measured or simulated motor efficiency maps [20, 25, 26], or measured power losses of the complete drivetrain [21]. The latter includes all

the losses from the inverter input to the wheel torque output, thereby incorporating transmission losses, and tire losses as well. The authors in [22] argue that the drivetrain power losses must be based on experimental measurements as opposed to complex formulations of power loss contributions from individual components (e.g. inverter, motor, transmission, tires...) that rely on parameter and variable estimations currently not available in production vehicles. However, fully or partially modeled drivetrain power losses offer advantages in terms of generality and ease of implementation for a variety of powertrain configurations. For example, in [17], the motor and inverter losses are modeled and validated experimentally using measured data. This motor-inverter pair can then be used to assess a variety of powertrain configurations in simulation.

Solution methods

The optimization method used to find the optimal torque distribution depends on real-time consideration. In [25], utilizing online optimization, it is recognized that the majority of the savings originate from the single- or two-axle drive as opposed to uneven torque distribution during two-axle drive, considering identical motors on the front and rear axle. Dynamic programming (DP) is used in [20], which is less suitable for real-time implementation as it requires complete knowledge of the drive cycle. DP is used rather as a benchmark to evaluate the performance of simpler distribution algorithms, or to generate look-up tables or distribution rules to be used online. Analytical solutions are fast and easily implemented, which is beneficial in terms of real-time implementation. In [17], the optimal front-to-rear distribution, in terms of minimal electric and longitudinal tire slip losses, is found analytically by expressing the inverter input power as a quadratic function of rear-to-total torque distribution ratio, k. The torque distribution is predominantly biased towards the front motor with higher overall efficiency, but varies with longitudinal acceleration. For positive accelerations, the distribution is increasingly shifted to the rear motors to reduce slip losses since longitudinal load transfer increases the vertical load in the rear. The opposite is true for negative accelerations, where the torque distribution is shifted to the front axle. The analytical solution is validated using experimental tests on road and in a test-bench.

An analytical expression for a torque threshold, beyond which the total torque is redistributed from a single axle drive to even distribution, is derived in [21]. Through the brute force approach, they find the threshold for different velocities based on experimental measurements of the entire drivetrain, resulting in a lookup table. The study performed by [22] supports the choice of simpler control allocation strategies. Three control allocation strategies are compared: explicit-, implicit- and hybrid control allocation, representing varying levels of complexity. Explicit control allocation is governed by a torque threshold between two powertrain operation modes, single axle and even distribution. The threshold is found through an analytical solution to the cubic approximation of measured drivetrain power losses as outlined in [21]. The implicit control allocation uses an offline optimization method and spline functions of the measured power loss data (thereby reducing the fitting errors of the cubic approximation) and stores the corresponding optimal torque distribution in a lookup table. Hybrid control allocation is a mix between the explicit and implicit approach in that the powertrain operation modes are limited to two, but the switch torque is found using piece-wise linear interpolation between data points. By analyzing the power losses between the strategies, the implicit scheme shows marginal improvements with respect to the simpler solutions provided by the explicit and hybrid algorithms. During experimental tests, the implicit algorithm introduces drivability issues and marginal increases in energy consumption due to the continuous variation of torque distribution.

Dependence on motor type

The resulting optimal torque distribution is inherently influenced by the type of motor, the efficiency characteristics of the motors, and whether the motors within the powertrain configuration are identical or not. For example, [25] uses 4 identical in-wheel brushless direct current motors and finds that single-axle drive is optimal for low torque demands, and four-wheel driving mode for high torque demands where the distribution is very close to even. In [21], the authors mathematically prove that, considering identical electric drivetrains with positive and strictly monotonically increasing power loss characteristics, two power-optimal drive modes are identified: single axle for low torque demands, and two axles equal distribution for high torque demands. The power loss characteristics are derived from switched reluctance motors, which have a cubic relationship to torque. In contrast, when identical permanent magnet synchronous motors (PMSM) are used, which are more quadratic in relation to torque, the torque should be equally distributed between the motors [12–14], at all times. Furthermore, as identified by [14], significant idle losses of the PMSM makes it impossible to improve the efficiency in the low-torque region by electrical means alone. The energy efficiency can be improved by 1) adding a coupling to mechanically disconnect the motor from the wheel, or 2) by exchanging the PMSM for a motor without a permanent magnet field and consequently smaller idling losses. With a coupling, the proposed torque distribution strategy leads to 4% reduction in energy consumption in the New European Driving Cycle (NEDC).

Energy-efficient torque vectoring

The minimization of energy consumption is typically evaluated in the longitudinal direction, i.e., using drive cycles like NEDC and WLTP defined by velocity profiles, thereby neglecting the energy consumed during cornering. Actively controlling non-critical vehicle behavior during cornering is commonly associated with drivability and "fun to drive"-elements as an understeered vehicle can adopt sportier behavior by reducing the understeer gradient using torque vectoring differentials [23] or multiple motors [18]. In the latter study, a direct yaw moment request is generated to follow a specific understeer characteristic, e.g., sportier than the baseline, and the torque distribution is optimized within the vehicle side to fulfill the yaw moment request. However, it was found that the input power to the motors decrease when the understeer gradient is reduced. This stands in contrast with the findings in [23] where the energy consumption was increased by 3% using a torque vectoring differential due to power losses associated with the actuation of the differential clutches. The energy savings seems to apply when individual motors are used to generate the differential torque.

The dependence on understeer gradient is related to losses generated during cornering, commonly referred to as cornering resistance. These losses arise due to lateral tire slip required for the lateral tire forces. A simple yet insightful simulation study is presented in [30], where the cornering resistance is minimized during steady state cornering by distributing the drive torque completely to the outer wheels, regardless if the vehicle is front-, rear-, or all-wheel driven. In [31], the effect of understeer characteristic on the power consumption is evaluated experimentally for steady state cornering. Six yaw rate references representing more or less understeer were tracked with torque vectoring for lateral accelerations ranging between 2 and 8 m/s^2, resulting in destabilizing and stabilizing direct yaw moments. The energy consumption is significantly reduced at higher lateral accelerations, reaching an impressive improvement of 12.3%, due to the combined effect of minimized motor losses and tire slip losses. The energy savings at lateral

accelerations representing moderate driving (2 m/s^2) are also quite significant, but mainly depend on favorable operation of the motors.

In [24], the optimal understeer characteristic is found for four power objectives separately: total power consumption, powertrain power losses, lateral slip losses, and longitudinal slip losses. The optimal understeer characteristic for lateral slip losses is close to neutralsteered, while the other three objectives favor a more understeered one. A study on the tire slip losses during cornering shows that the tire slip velocity vectors should be equal to minimize the tire slip power loss, leading to equal utilization of the tire work load [32]. During moderate driving, this leads to approximately 2% reduction in total tire slip power losses.

Other objective functions

The control allocation formulation is not limited to power loss minimization. For example, in [33], it is applied to improve vehicle stability during lateral maneuvers by preventing tire saturation. In this case, the objective function in (1.1) is replaced by a quadratic cost that penalizes actuators experiencing high combined slip and/or low vertical load, i.e., conditions under which the remaining tire force potential is reduced. A similar objective is pursued in [34], where the formulation is extended to include energy consumption minimization and is integrated within an MPC framework. The resulting torque distribution is evaluated only during a sine-with-dwell maneuver, which is highly dynamic in nature. In this scenario, the required direct yaw moment is generated by propelling one side of the vehicle while braking the other. Such torque distributions are not found in energy-oriented control allocation, as (1) simultaneous propulsion and braking are inherently inefficient [21], and (2) motion requests requiring differential torque of such magnitude are rarely generated. However, as shown in [32], tire power losses can be minimized when tire slip is equalized across all four wheels, an approach that not only reduces energy consumption but also balances tire workload, which contributes to improved vehicle stability.

Transmission

Apart from energy-efficient torque distribution, the transmission introduces further opportunities to reduce energy consumption, as it can increase the operational flexibility of the electric motors. The choice of transmission ratio is typically a trade-off between acceleration performance, i.e., maximum torque, and top speed. With multiple gears, this trade-off is facilitated. Furthermore, it could potentially lead to improved energy efficiency compared to the powertrain configuration consisting of a single motor with a one-speed gearbox commonly used in BEVs.

In [35], multiple transmission types are investigated for a vehicle with one motor, including one- and two-speed gearboxes and variable transmission ratio. The variable transmission ratio presents the greatest potential to reduce energy consumption. In contrast, [36] finds that a powertrain with a two-speed gearbox leads to the lowest energy consumption. The authors in [37] compare four powertrain configurations: single motor one-speed gearbox, single motor two-speed gearbox, dual motors with a one-speed gearbox each, and dual motors with a two-speed gearbox each. They find that the powertrain configuration consisting of dual motors with one-speed gearboxes is the best for energy consumption, as more complex gearboxes increase vehicle weight, ultimately canceling the gains from improved powertrain efficiency by increased mass to move.

Furthermore, the ratio of one-speed gearboxes can be jointly optimized with torque distribution. In [38], optimization of transmission ratio for two one-speed gearboxes, each connected to an electric motor powering the same axle, is performed in combination with optimization of torque distribution. To maximize energy efficiency, both transmission ratios should be minimized, while to maximize acceleration performance, here measured in terms of acceleration time, the transmission ratios should be maximized. The energy consumption is improved by 11.2% compared to a powertrain consisting of one motor with one-speed gearbox.

1.1.2 Energy efficient velocity trajectories

Additional opportunities to reduce energy consumption arise with intelligent algorithms planning the velocity trajectory to maximize energy efficiency. To increase the range of BEVs, the authors in [39] develop an eco-driving function that is experimentally evaluated in an urban environment, effectively leading to a 14.1% reduction in energy consumption. In [40], a DP-generated velocity profile reduces the energy consumption by 9.8% compared to the profile of the average driver. The authors in [41] show, using DP, that energy-efficient driving for BEVs may result in Pulse-and-Glide (PnG) at high frequencies, which is a well-known eco-driving mechanism for ICE vehicles [42]. The energy consumption is reduced significantly, with greater savings in the lower speed range (< 20 km/h). The PnG strategy is also found in [43], though at lower frequencies since minimizing the longitudinal jerk is part of the objective function of the optimization problem.

The joint optimization of torque distribution and velocity trajectory can yield further energy savings in overactuated vehicles. For example, [43] demonstrates that the joint optimization for an electric powertrain with two motors reduces the energy consumption by 8.8% compared to a single-motor configuration. In [44], the joint approach is compared to only optimizing the torque distribution between ICE and electric motor in a HEV. By allowing the velocity to deviate by 0.5 m/s from the reference, the electric cost is reduced by 14.77%, compared to strictly following the reference velocity while only optimizing the power split. Other studies regarding overactuated BEVs address these two subproblems individually. The authors in [45], for example, divide the problem in an upper layer, finding a velocity profile that minimizes the battery power based on the total torque of the motors, and a lower layer, finding an energy-optimal torque distribution. The layered approach is also applied in [46], where the higher level determining the speed profile penalizes the rate of change of the desired acceleration to improve energy efficiency. Similar to previous work, the torque distribution is addressed in a lower layer. The resulting hierarchical function architecture is beneficial in terms of adaptability and flexibility for the automotive industry. New technologies and manufacturers emerge rapidly, and increased autonomy and connectivity of cars put tremendous demands on the automotive manufacturers to reduce development costs related to the control architecture of each new vehicle. If a function could be reused when developing a new vehicle configuration, development costs would be instantly reduced.

1.2 Research questions

Based on the literature review presented in the previous section, the research questions addressed in this thesis are formulated accordingly,

RQ1. What are the energy consequences of a hierarchical functional decomposition, i.e., separating the optimization of longitudinal velocity trajectory and torque distribution, in overactuated battery electric vehicles? (Paper D)

The first research question addresses the close relationship between velocity trajectories and powertrain operation that has previously been addressed either separately or jointly. There is a gap in research as to how the separation of the EMP affects the potential to reduce the energy consumption. The aim is to quantify the effects in terms of energy consumption for a predetermined road segment, and identify dependencies on velocity and road grade. The study is conceptual, i.e., not designed for real-time implementation.

RQ2. How can the optimization of velocity trajectory be augmented with information about the combined powertrain efficiency, without increasing the number of optimization variables, to mitigate the energy consequences associated with decoupling velocity planning from torque distribution? (Paper D)

Because of the possible benefits of a hierarchical function architecture concerning re-usability and computational effort, the second research question addresses how such a separation can be achieved with minimal impact on the potential to reduce energy consumption. Can the effects be mitigated if the predictive layer has information on the combined efficiency of the powertrain? In what way should this information be conveyed? The solution explored in this work involves a power loss map for the combined powertrain, defined on a vehicular level in terms of longitudinal force and velocity. The power loss map is incorporated in the optimization of velocity trajectory, and the results are compared to the sequential and joint solution of the EMP.

RQ3. How to coordinate actuators, i.e., allocate individual motor torques and determine coupling/decoupling of motors, to minimize power losses and at the same time follow the driver's intention on vehicle motion? (Papers A & C)

The third research question addresses the torque distribution and control of couplings to minimize power losses in the electric drivetrain and in the tires. The research is divided into two parts:
(1) Front-to-rear distribution
Previous work on the topic is extended with real-time implementable algorithms, including the power-optimal management of couplings, for a vehicle with four PMSMs. Furthermore, the effect of tire-related losses on energy consumption is quantified for moderate driving.
(2) Left-to-right distribution
A detailed analysis on how to minimize lateral slip power losses with a direct yaw moment, independent of powertrain configuration, and its effect on energy consumption during moderate driving is missing in research. For example, [31] includes powertrain losses, and [32] and [30] do

not consider the total energy consumption. Additionally, the dependence on understeer gradient of the passive vehicle is explored.

RQ4. How do different transmission ratios, when combined with power-optimal torque distribution, affect the potential for minimizing energy consumption in battery electric vehicles? (Paper B)

The fourth research question addresses the operational region of the motors specifically. Optimization of torque distribution and velocity trajectory both aim to guide the powertrain to more efficient operating regions of the motors. Both are related to software. Hardware parameters, such as the transmission ratio, reshapes the motor map from a vehicular perspective. The objective is to identify the optimal transmission ratios, when combined with power-optimal torque distribution, for a vehicle equipped with multiple PMSMs and couplings, and quantify the impact on energy consumption.

1.3 Limitations

Energy consumption can be evaluated in many different driving situations, which could be more or less relevant for the everyday driver. For example, energy can be minimized in an extreme maneuver with great energy savings but will not benefit the energy consumption in any, for user or society, important way since this maneuver seldom occurs. As a result, moderate driving is considered in this thesis with average lateral and longitudinal accelerations typically below 2-3 m/s^2. In addition, the following limitations are considered in this thesis.

- The focus is on the transfer of energy within a BEV, i.e., the energy flow between electrical grid and vehicle is not included in this thesis.
- Experimental tests not performed to validate findings from simulation.
- High road-tire friction is assumed, $\mu = 1$.
- The interaction of the developed energy-efficient algorithms with existing vehicle functions, such as stability systems, is not considered.
- Only forward driving is studied, $v_x \geq 0$.
- Actuator dynamics is neglected, and low-level actuator control is assumed to be ideal, i.e., the requested motor torque is provided without any delay.
- Ideal working conditions for the motors: the influence of temperature on power losses is not included.
- Ideal working conditions for the battery: the influence of temperature and state of charge (SOC) on internal resistance is not included.

1.4 Scientific contribution

The scientific contribution of this thesis includes:

- Quantifying the energy consequences of a hierarchical function architecture in velocity trajectory planning and actuator coordination. Specifically, the effect of separating the optimization of velocity profile and torque distribution on energy consumption (Paper D).
- Presenting a method to improve the separated EMP that provides similar results as the comprehensive problem of energy-optimal velocity planning and torque distribution. In other words, a method to enable a hierarchical function architecture with minimized effects on the potential to minimize energy consumption (Paper D).
- The design of two real-time implementable algorithms to handle power-optimal torque distribution and coupling scheme for multiple permanent magnet synchronous motors, and quantifying the effect on energy consumption (Paper A).
- Exploring the joint optimization of hardware parameters and software, and quantifying the effect on energy consumption. Specifically, optimizing the transmission ratios for individual single-speed gearboxes in combination with the optimization of torque distribution, with and without couplings present (Paper B).
- A separate analysis, excluding the powertrain, on how lateral tire slip losses are influenced by a direct yaw moment during moderate cornering, focusing on its dependence on understeer gradient and its impact on overall power consumption. Specifically, the direct yaw moment required to minimize lateral tire slip losses is analytically derived for a range of understeer gradients, and the resulting savings in tire slip losses are evaluated relative to the total power consumption of the vehicle (Paper C).

1.5 Thesis outline

The outline of the thesis is as follows. In Chapter 2, the problem of optimizing energy consumption is presented, in addition to the power losses minimized in this thesis. Furthermore, an introduction to the optimization methods employed is provided. Then, the results of the conducted research is presented, divided into two parts. The first part, presented in Chapter 3, concerns the energy consequences of separating the EMP in a hierarchical control architecture. The previously presented optimization methods are applied to the specific problem formulation, and the effects on velocity profile and energy consumption are evaluated. The second part, presented in Chapter 4, is focused on power-efficient torque distribution, where the individual contributions on energy consumption of the following are studied: (1) coupling/decoupling idle motors, (2) different transmission ratios on front and rear axle, and (3) tire power losses. The concluding remarks are provided in Chapter 5. Finally, directions for future work are presented in Chapter 6, closing this thesis.

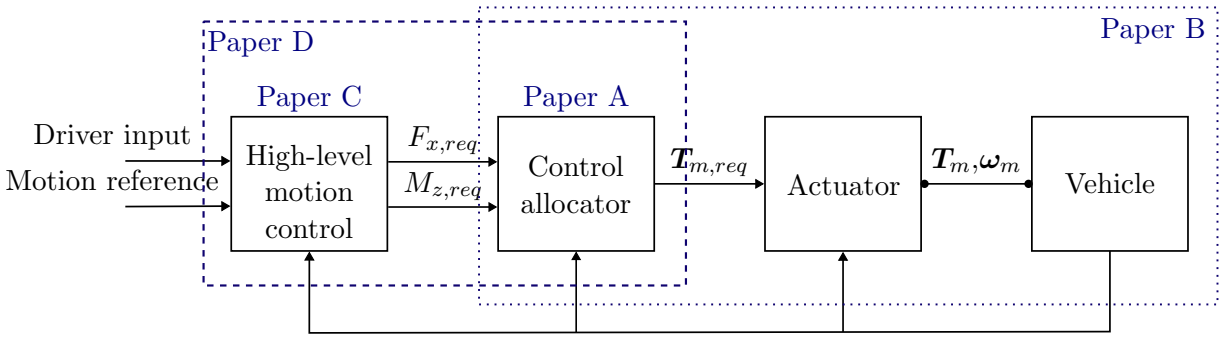

Figure 1.2: *Generalized control architecture for electric propulsion used in literature. The contribution of each appended paper is highlighted.*

1.6 Summary of appended papers

The appended Papers each address different aspects of the generalized control architecture, illustrated in Figure 1.2. Paper A focuses on the control allocator, exploring different torque distribution strategies and their effect on energy consumption. Paper B extends this by jointly optimizing the transmission ratio on the front and rear axles in addition to torque distribution, thereby combining the optimization of software and hardware. Paper C shifts focus to high-level motion control, examining energy-efficient direct yaw moments and their relationship to understeer characteristics. Finally, Paper D evaluates the energy consequences of adopting a hierarchical function architecture, in which the high-level motion control and control allocator are separated, as shown in Figure 1.2. The paper also proposes a method to mitigate the resulting energy consequences. More detailed summaries of each paper are provided below.

Paper A, front-to-rear power-optimal torque distribution with couplings

In Paper A, different strategies for instantaneous front-to-rear torque allocation are evaluated. A conventional passenger vehicle with four identical PMSMs, one for each wheel, is considered. Two optimization-based control allocation schemes including offline and online optimization are compared to fixed distribution strategies, and distribution based on equal friction utilization. The control of a coupling to mechanically disconnect the motors from the wheels is included, allowing for quantification of the effect of removing the motors' idle losses on energy consumption. The objective of the optimization is to minimize power losses related to torque distribution while fulfilling the driver's request on vehicle motion. The power losses constituting the objective function of the optimization problem include modeled longitudinal tire slip and rolling resistance losses, and experimentally measured electric losses in the motor and inverter. The offline optimization scheme involves finding the optimal torque distribution through a brute force approach, resulting in a lookup table (LUT) implemented online in simulation. The online optimization scheme is based on quadratic programming (QP), where the power losses are formulated as quadratic expressions of torque. By neglecting the limits on motor torque in the form of inequality constraints, the quadratic program can be solved analytically, facilitating online implementation. To evaluate the effect on everyday driving, a moderate driver model defined in CarMaker is used to complete the Gothenburg City Cycle (GCC), a drive cycle designed to represent everyday driving. The results show that the ability to decouple the motors accounts for the majority of the reduction in energy consumption: 3.9% energy is saved compared to 0.2% without couplings.

Paper B, joint optimization of transmission ratios and torque distribution

In Paper A, it was found that the greatest potential to reduce energy consumption lies in the ability to mechanically decouple the motors from the wheels. This led to the question whether different transmission ratios on the front and rear axle can increase this potential further, as it dictates to some extent the operating domain of the electric motors. Thus, in Paper B, the optimal transmission ratios on the front and rear motors are determined for the same vehicle considered in Paper A. The optimization is approached using the brute force method, where the front and rear transmission ratios range between 6 and 14 in steps of 2. For every transmission ratio combination, GCC is run with three different torque distribution strategies: even wheel torque distribution, power-optimal torque distribution without couplings, and power-optimal torque distribution with couplings. The QP-based algorithm is used as an optimization method for torque distribution. Furthermore, to extend the control allocation problem, wheel angles are included as control variables. It is found that the optimal front-to-rear transmission ratio depends on torque distribution strategy, and that by optimizing the front-to-rear ratios, the energy consumption can be reduced by 8.4% compared to the original transmission ratio of 10 on all motors and an even torque distribution. Minimal torque vectoring left-to-right was seen as the model generating the yaw moment request was parameterized to mimic the behavior of the high-fidelity model in IPG CarMaker.

Paper C, upper bounds on lateral tire slip losses during moderate driving

In Paper C, a power-optimal direct yaw moment request independent of powertrain configuration for moderate driving is found. Again, the QP is used to find the direct yaw moment request that minimizes the lateral slip power losses for a front-wheel-steered, linear single-track model. It is found that the optimal direct yaw moment, M_{dir}^*, makes the front and rear lateral slip angles equal, consequently making the vehicle neutral-steered. The resulting M_{dir}^* is validated using a high-fidelity model in IPG CarMaker in moderate steady state cornering, $a_y = 2$ m/s^2, coinciding with the minimum in lateral tire slip losses reported the software. To explore the dependence of M_{dir}^* on understeer gradient, different understeer gradients are realized by tuning the lateral tire stiffness of the front and rear tires in both the single-track and CarMaker model with the total lateral stiffness unchanged. As depicted by the analytical solution, M_{dir}^* is destabilizing for understeered vehicles, and stabilizing for oversteered vehicles, guiding the vehicle to neutral-steered behavior. The reduction in lateral slip power loss using M_{dir}^* ranges between 0.4-2.9% compared to $M_{dir} = 0$, where the savings increase with the magnitude of the understeer gradient. However, the savings do not translate to significant reductions considering the total power consumption of the vehicle, partly because of longitudinal tire slip losses arising in the generation of M_{dir}^*. Through simulated calibration of M_{dir}^* to minimize the total tire slip losses, i.e., both longitudinal and lateral tire slip losses, and focusing on the total power consumption of the vehicle (powertrain excluded), the savings reduced to 0-0.1% compared to $M_{dir} = 0$, which could be deemed negligible.

Paper D, energy consequences of decoupling the optimization of velocity trajectory and torque distribution

In Papers A and B, control allocation is used which assumes that the task of vehicle motion control and actuator selection can be separated. Paper D analyzes this separation in terms of energy, applied to the optimal control problem (OCP) of energy-efficient longitudinal velocity trajectories and torque distribution. The comprehensive EMP, in which the OCP solves for

both the velocity profile and torque distribution, is compared to a layered approach in which the OCP only solves for the velocity profile and the optimization of torque distribution is computed instantaneously. In the layered approach, the OCP generates a longitudinal torque request to be fulfilled by the instantaneous torque distribution, the latter representing the control allocator used in Papers A and B. The two resulting optimization architectures are referred to as the centralized (CA), and de-centralized architecture (DCA), respectively. Furthermore, to enable the separation with minimal energy consequences, a third variant of the problem formulation is suggested which represents a midway between CA and DCA, referred to as the refined de-centralized architecture (r-DCA). In this variant, the OCP of DCA is augmented with an aggregated power loss map, generated using the optimal torque distribution for the vehicle operational domain. The augmented power loss map is formulated in terms of vehicular longitudinal force and velocity, leading to a separation of the vehicle motion and the powertrain layout in that the OCP does not need specific information on the number of motors except for their combined capabilities. The results show that the energy consequences depend on velocity, where the consequences are greater at lower velocities but negligible at higher velocities. At low velocities, the DCA increases energy consumption by 3.5% compared to CA. The aggregated power loss map in r-DCA manages to mitigate some of these consequences, reducing the increase in energy consumption to 0.4% compared to CA. The resulting velocity profile suggests that the velocity should be increased at lower velocities to reach more efficient operating regions of the motors.

2

Optimization of energy consumption

To solve the EMP addressed in this thesis, both predictive and instantaneous optimization methods are used depending on whether the problem is treated in parts of as a whole. This chapter outlines the adopted methodology, including the derivation of the energy consumption model, the power losses targeted through deliberate torque distribution, and the optimization methods applied. Detailed implementation of the predictive and instantaneous methods is presented in Chapters 3 and 4.

2.1 Energy consumption

The energy consumption of a BEV corresponds to the electrochemical energy drained from or supplied to (through regeneration) the battery,

$$E = \int_{t_0}^{t_f} P_b(t)dt \tag{2.1}$$

where $P_b(t)$ represents the electrochemical power. However, not all of this power is converted into the vehicle's kinetic energy; some is used to power auxiliary devices, and some is lost in the conversion into mechanical energy. The energy lost is primarily due to internal resistance in the battery, electrical and friction losses in the motors and inverters, friction in the transmission and tire losses. The power flow in the drivetrain is illustrated in Figure 2.1.

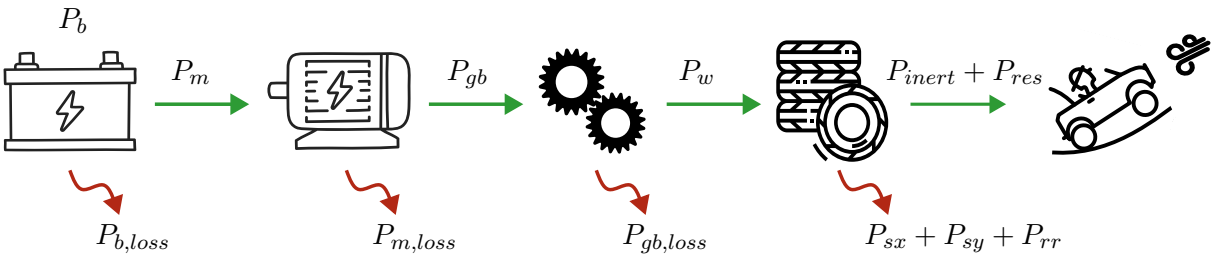

Figure 2.1: *Drivetrain power flow.*

Auxiliary power sinks, primarily attributed to HVAC systems, were assumed negligible in this work. This assumption is debatable since auxiliary devices can consume approximately 20 Wh/km at 15–20 °C. [47]. If included in the calculation of total energy consumption, the energy consumption reported in this thesis would increase, slightly reducing the percentages used for comparison between torque distribution strategies. However, the main source of auxiliary power consumption, the HVAC system, is not affected by powertrain operation but rather by environmental conditions such as temperature. Therefore, the differences in absolute energy

consumption remain unchanged, as they depend on the power consumption of the drivetrain. Other power sinks, such as losses in power links, are disregarded in this analysis.

2.1.1 Battery

Initially, power is lost due to internal resistance in the battery. The power losses are typically simplified or neglected in eco-driving studies for electric vehicles [41, 43, 48]. In case of predictive optimization, which decides the total power demand, the battery efficiency can influence the solution, especially during cold climates or low state-of-charge (SOC). Here, it is assumed that the battery is ideally conditioned, meaning that it operates at an optimal temperature and that the SOC stays within limits such that the internal resistance can be considered constant. Under these conditions, the battery losses are significantly smaller than the losses in the motor pair as shown in the analysis presented in Appendix A. Furthermore, the batteries in modern cars have reduced internal resistance and higher voltage, leading to higher battery efficiency. The battery losses have an impact on range, but their effects on the optimized vehicle speed profile is neglected. Therefore, it is assumed that $P_b = P_m$.

In Papers A and B, where the energy consumption for an everyday drive cycle is evaluated, a round-trip efficiency of 95% is used for the battery [49] to provide a more accurate consumption estimate. The electrochemical power is then expressed as,

$$P_b = \begin{cases} \sqrt{\eta_{b,rte}} P_m, & \text{if } P_b \leq 0 \\ \sqrt{\frac{1}{\eta_{b,rte}}} P_m, & \text{if } P_b > 0 \end{cases} \tag{2.2}$$

where $\eta_{b,rte}$ is the battery efficiency and P_m motor power. It is assumed that all motors are supplied with power from one common battery, and that battery loss is relatively independent of distribution as found in [13].

2.1.2 Electric motor and inverter

The electric motor and inverter are considered as one unit in this thesis, simply referred to as the motor. The power losses originate from heating of electric components (resistors, capacitors, etc.), magnetic losses in the windings and core of the motors, and friction. Two types of electric motor are considered: the asynchronous motor (ASM) and permanent magnet synchronous motor (PMSM). The ASM is generally less efficient than the PMSM, but has the advantage that it can be electrically switched off to avoid idle losses since the magnetic field is created by current and not by permanent magnets. The PMSM, as the name implies, has permanent magnets embedded leading to a permanent magnetic field. During driving, even though the motor does not supply any torque, it generates significant power losses when the magnetic field is rotating. To avoid these losses, the motor must be mechanically disconnected from the wheels to stop the rotation.

The power losses of the PMSM used in Papers A, B and C are experimentally measured in a test-bench. The power losses of the ASM and PMSM in Paper D are acquired through simulation of high-fidelity models. It is assumed that the motors exhibit ideal cooling, thereby neglecting temperature dependent variation in power losses. This assumption is supported by the findings in [22], where the motor temperature did not influence the power losses resulting from experimental measurements in any significant way. The corresponding efficiency maps of the three motors can

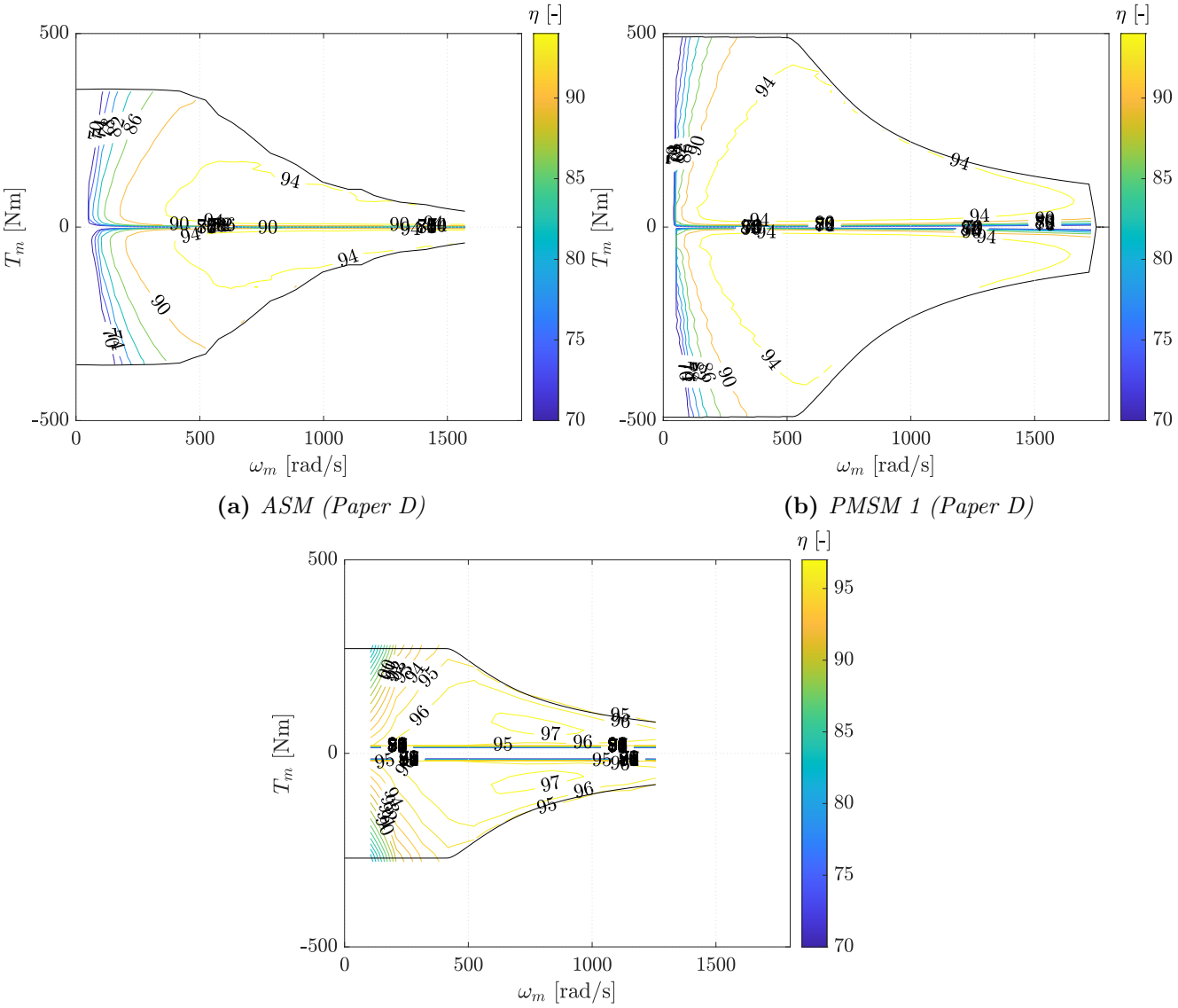

(a) *ASM (Paper D)*

(b) *PMSM 1 (Paper D)*

(c) *PMSM 2 (Papers A, B and C)*

Figure 2.2: *Efficiency maps of electric motors used in this thesis.*

be seen in Figure 2.2.

The total power consumption of the motors is expressed accordingly,

$$P_m = \sum_{k=1}^{p} (P_{gb,k} + P_{m,loss,k}) \tag{2.3}$$

where $P_{gb,k}$ represents the power transferred to the gearbox, $P_{m,loss,k}$ is the power loss of motor $k \in \{1, ..., p\}$ where p is the number of motors.

2.1.3 Gearbox

The power lost in the gearbox origin from friction in the gears. It can be expressed as,

$$P_{gb,k} = P_{w,k} + P_{gb,loss,k} \tag{2.4}$$

where $P_{w,k}$ is the power transferred to the wheels and $P_{gb,loss,k}$ is the power lost in the gearbox according to,

$$P_{gb,loss,k} = (1 - \eta_{gb})|P_{w,k}| \tag{2.5}$$

where η_{gb} is the gearbox efficiency. In the case of one motor per wheel ($k \in \{1, \ldots, 4\}$), $P_{w,k}$ represents the power at each individual wheel. However, with one motor per axle ($k \in \{1, 2\}$), the power from the gearbox is distributed between the two wheels on the same axle; for example, on the front axle, $P_{w,1} = P_{w,f,left} + P_{w,f,right}$. In Paper A, a fixed gear efficiency is used while in Paper B the power losses in the gearbox are derived from measurements. The vehicle model in Papers C and D is simplified where the transmission losses are neglected since these papers are more concept oriented rather than evaluating everyday energy consumption.

2.1.4 Power at the wheels

The total power is represented by the sum of the power produced at the wheels.

$$P_{w,tot} = \sum_{i=1}^{4} P_{w,i} = P_{inert} + P_{res} + P_{rr} + P_{sy} + P_{sx} \tag{2.6}$$

where $P_{w,i}$ is the power produced at wheel $i \in \{1, ..., 4\}$, P_{inert} represents inertial power required to initiate a change in kinetic energy, P_{res} represents power of aerodynamic and grade resistance, P_{rr} represents rolling resistance, and P_{sy} and P_{sx} represent power lost due to lateral and longitudinal slip, respectively. A full derivation of the total power is given in Appendix B.

Finally, the total power drawn from the battery, assuming $P_b = P_m$, is found by combining (2.3)-(2.6),

$$P_b = \sum_{k=1}^{p} (P_{m,loss,k} + P_{gb,loss,k}) + P_{inert} + P_{res} + P_{rr} + P_{sy} + P_{sx} \tag{2.7}$$

2.2 Modeling power losses in the powertrain and tires

The power losses in the drivetrain are mainly dependent on two factors: (1) the total power demand, and (2) how the available actuators are used to fulfill the total power demand. The total power demand is governed by the motion of the vehicle, i.e., its velocity trajectory, which in turn is determined by a driver (human or autonomous), or an algorithm. One part of this thesis handles the generation of total power demand, but this section is dedicated to how to fulfill that demand while minimizing the energy consumption. Specifically, the power losses influenced by motor torque are derived and presented here.

Power losses are chosen as opposed to efficiency commonly used in literature [50–52]. Efficiency is not a practical measure, as it is not well defined at zero power (zero torque or speed). It is useful for illustrative purposes to identify the location of efficient operating regions of, e.g., an

electric motor. However, for electric vehicles, this measure is ill-suited for evaluating energy consumption, as it overlooks power losses that occur at zero power output, potentially leading to suboptimal solutions. In fact, such an occurrence was discovered in [12], where the optimal torque distribution derived using motor efficiency provided positive results in simulation but did not lead to a reduction in energy consumption in road vehicle tests.

2.2.1 Powertrain power losses

The largest contributor, and the share affected by deliberate torque distribution the most, is the power losses in the motors (including inverters, as declared prior). How to distribute the total torque demand among available motors is not straightforward, as the power losses are non-linearly dependent on motor torque and rotational speed. The power losses are incorporated in the objective function of the optimization problems presented later in Section 2.3 through polynomial approximations,

$$P_{m,loss}(T_m, \omega_m) = \sum_{i=1}^{e} \sum_{j=1}^{f} h_{i,j} (\omega_m)^e (T_m)^f \tag{2.8}$$

where e and f represents the order of the polynomial fit for ω_m and T_m, respectively, and $h_{i,j}$ the fitting coefficients. The order of the fit varies with optimization method and motor power loss maps: in Paper D, $e = 5$ and $f = 4$, while in Papers A, B and C $e = f = 2$ due the use of a quadratic program and quadratic nature of the power losses related to the motor considered in these studies.

2.2.2 Tire power losses

Tire power losses arise when rubber elements in the tire deflect. The deflection is essential in the generation of tire forces in the longitudinal and lateral direction, required to induce motion. Although vertical deflection of the tire improves occupant comfort to some extent, it is generally undesired as it gives rise to rolling resistance.

Rolling resistance power loss

Rolling resistance occurs due to hysteresis in the tire, i.e., the deformation energy is greater than the recovery energy. It is always present in a rolling tire. The rubber elements in a rotating tire deflect upon coming into contact with the ground, and builds up a storage of potential energy due to its flexibility. As the rubber element travels through the contact patch and leaves it, it will spring back out and regain its shape. However, due to damping in the rubber, some of the potential energy is converted into heat and is thereby lost. Rolling resistance is commonly modeled as a wheel torque opposing the direction of rotation, calculated by multiplying the normal load with a rolling resistance coefficient (as in Appendix B) that depends on factors such as load, tire construction, and tire pressure. A more elaborate model is given by the well-known Magic Formula tire model, modeling the rolling resistance moment (neglecting camber, and load and pressure dependencies on the rolling resistance coefficient) according to [53],

$$M_{y,i} = -F_{z,i} r_0 \left\{ q_{sy1} + q_{sy2} \frac{F_{x,i}}{F_{z0}} + q_{sy3} \left| \frac{v_{x,i}}{v_{ref}} \right| + q_{sy4} \left(\frac{v_{x,i}}{v_{ref}} \right)^4 \right\} \tag{2.9}$$

where $F_{z,i}$ represents the tire vertical load, $F_{x,i}$ the tire longitudinal force, $v_{x,i}$ the longitudinal velocity of the wheel center, and the remaining parameters r_0, $q_{sy1} - q_{sy4}$, F_{z0} and v_{ref} are acquired during experimental tire measurement. Thereby, the power lost due to rolling resistance is given by,

$$P_{rr} = \sum_{i=1}^{4} -M_{y,i}\omega_{w,i} \tag{2.10}$$

where $\omega_{w,i}$ represents rotational velocity of the wheel. As can be observed in (2.9), the rolling resistance moment is mainly dependent on normal load and velocity. The parameter q_{sy2} determining the influence of applied torque on P_{rr} is hard to find, as it is often neglected and literature concerning the effect of applied torque on rolling resistance is very limited [54]. Here, it is derived from [55] for a tire with 400 kg in normal load.

Longitudinal tire slip power loss

The deflection of rubber elements in the longitudinal direction is caused by a difference in tire tangential speed and longitudinal speed of the wheel center relative to the ground, i.e., tire slip, of the contact patch. The surface of the rubber elements sticking to the ground in the contact patch will follow the global vehicle longitudinal velocity while the upper part of the rubber element will follow the rotational velocity of the tire. Depending on whether propulsive or braking torque is applied, the tangential speed of the tire will be greater or smaller than the speed of the wheel center, leading to positive or negative slip. The rubber element acts like a spring, and as it is deformed, shear stress develops which generates a force. Depending on tire stiffness, more or less deflection (i.e. tire slip) of the rubber elements is needed to produce the same longitudinal force. Tire slip is necessary for forces to develop, but it also leads to a power loss referred to as longitudinal slip power loss,

$$P_{sx} = \sum_{i=1}^{4} F_{x,i}\kappa_i v_{x,i} \tag{2.11}$$

where $F_{x,i}$ represents the longitudinal force of tire $i \in \{1, 4\}$, κ_i the longitudinal tire slip, and $v_{x,i}$ the wheel corner velocity. For a full derivation, see Appendix B. Assuming a linear tire model, $F_{x,i} = C_{x,i}\kappa_i$, (2.11) can be rewritten accordingly,

$$P_{sx} = \sum_{i=1}^{4} C_{x,i}\kappa_i^2 v_{x,i} \tag{2.12}$$

Assuming steady state driving, i.e., the tire stiffness can be regarded as constant, the longitudinal slip loss is minimized when κ_i is minimized on each individual wheel according to (2.12). In practice, this translates to distributing torque to wheels with higher tire stiffness provided that the required total longitudinal force does not change. The torque could for example be biased towards the axle with higher normal load under the condition that all wheel corners have the same tire.

Lateral tire slip power loss

In the lateral direction, the difference between the angle and the direction of travel of the wheel, i.e., the slip angle, causes lateral deflection of the rubber elements. It can be expressed as the

lateral force multiplied by lateral wheel velocity,

$$P_{sy} = \sum_{i=1}^{4} F_{y,i} v_{yw,i} \tag{2.13}$$

where $v_{yw,i}$ is the lateral velocity in the wheel coordinate system. Assuming a linear tire model, the lateral force can be expressed as a product of lateral tire stiffness and slip angle according to,

$$F_{y,i} = -C_{y,i}\alpha_i \tag{2.14}$$

$$\text{where } \tan\alpha_i \approx \alpha_i = \frac{v_{yw,i}}{v_{xw,i}} \tag{2.15}$$

Combining (2.13), (2.14) and (2.15), the total lateral tire slip power loss can be written as

$$P_{sy} = \sum_{i=1}^{4} C_{y,i}\alpha_i^2 v_{xw,i} \tag{2.16}$$

By adopting the one-track model, i.e., assuming the same slip between the tires on the front and rear axle (α_f and α_r) and the same lateral tire stiffness ($C_{y,f}$ and $C_{y,r}$), assuming small angles and $v_{xw,i} \approx v_x$, (2.16) can be rewritten as

$$P_{sy} = \left(F_{y,f}\alpha_f + F_{y,r}\alpha_r\right) v_x \tag{2.17}$$

The derivation of lateral power slip loss can also be approached from a complete vehicle reference frame, as in Appendix B. Steering of the wheels is necessary for the deflection to occur, thereby generating lateral forces, but it will also contribute to a force working against the direction of motion of the vehicle referred to as *cornering resistance*. Comparing (2.17) to the expression for cornering resistance in (B.16), one can observe that they are equal, i.e., $P_{sy} = P_{cr}$.

According to (2.16), the lateral tire slip losses are dependent on lateral tire stiffness and lateral slip. The lateral tire stiffness generally reduces with the lateral load transfer which occurs during cornering. Assuming steady state cornering, i.e., a constant lateral load transfer, the lateral tire stiffness can be regarded as constant. The lateral tire slip losses are then minimized when the lateral slip is minimized on each axle. In contrast to the longitudinal direction, where the wheel's longitudinal force can be controlled directly through torque distribution, the control of lateral forces is more subtle. During cornering, the vehicle's lateral and yaw motions are governed by the sum of lateral forces and their balance. The sum of lateral forces arises to provide the required lateral acceleration, which is determined by the forward velocity and the curve radius. The balance between front and rear lateral forces is determined by vehicle parameters, specifically the distances from the center of gravity to the front and rear axles denoted as l_f and l_r, respectively. This balance can be influenced by the application of a direct yaw moment through,

$$M_{dir} = F_{yr} l_r - F_{yf} l_f \tag{2.18}$$

With $M_{dir} > 0$, the proportion of the rear lateral force F_{yr} increases, and with $M_{dir} < 0$, the proportion of the front lateral force F_{yr} increases. In extension, the lateral tire slip losses are influenced as the lateral force is a product of lateral tire stiffness and lateral slip (2.14).

2.3 Optimization methods

An optimization problem is given by the general form,

$$\min_{x \in \mathbb{R}^n} \quad f(x) \tag{2.19}$$

$$\text{such that} \quad h(x) = 0_m \tag{2.20}$$

$$g(x) \leq 0_q \tag{2.21}$$

where x represents the optimization variables, $f : \mathbb{R}^n \to \mathbb{R}$ is an objective function (or cost function) to be minimized, $h : \mathbb{R}^n \to \mathbb{R}^m$ represents equality constraints, and $g : \mathbb{R}^n \to \mathbb{R}^q$ inequality constraints. Depending on whether the problem context is time-dependent or time-independent, the optimization is either predictive (dynamic) or instantaneous (steady state), respectively. In this thesis, both techniques are used with the objective to minimize energy consumption. A fundamental difference in the structure of the objective function between the predictive and instantaneous optimization problems is that *energy* is minimized predictively, whereas *power* is minimized instantaneously, as dictated by the length of the optimization horizon. In the predictive case, it encompasses the entire road segment, whereas in the instantaneous case, it is limited to the current sample.

2.3.1 Predictive energy optimization: optimal control problem (OCP)

The predictive optimization technique is applied to the problem of finding an energy-optimal velocity trajectory. Various methods within the predictive optimization framework utilize a receding horizon, for example MPC, which enables the solution trajectory to be updated based on unforeseen future events or uncertainties. The purpose of the work here, in which the predictive optimization is used, is conceptual rather than intended for real-time implementation. To this end, the optimization problem is solved once for the complete horizon. In other words, it is assumed that the surrounding environment will not change during the time it takes to cover the road segment, and that the model defined in the predictive optimization problem perfectly captures the behavior of the vehicle plant, which is true in this case as they are equal. Here, the general predictive optimization problem is defined, and its specific application is further presented in Chapter 3.

The task of finding the energy-optimal velocity profile is formulated as an optimal control problem (OCP) with the objective to minimize the energy consumption traveling from an initial point s_0 to a final point s_f,

$$\min_{\boldsymbol{x}(s), \boldsymbol{u}(s)} \int_{s_0}^{s_f} F_m(\boldsymbol{x}(s), \boldsymbol{u}(s)) ds \tag{2.22}$$

$$\text{such that} \quad \dot{\boldsymbol{x}}(s) = f(\boldsymbol{x}(s), \boldsymbol{u}(s)) \tag{2.23}$$

$$\boldsymbol{x}(s) \in \mathbb{X} \tag{2.24}$$

$$\boldsymbol{u}(s) \in \mathbb{U} \tag{2.25}$$

where the independent variable s represents distance, $\boldsymbol{x}(s)$ is a vector containing the state variables, $\boldsymbol{u}(s)$ a vector containing the control variables, $F_m(\cdot)$ the total force equivalent to the power generated by the motors, $f(\cdot)$ the dynamics of the state variables, and $\mathbb{X}$ and $\mathbb{U}$ the feasible sets of the state and control variables respectively. Distance is chosen as the independent

variable as opposed to time, as road information, e.g., topography, is usually provided in terms of space.

The state vector is chosen as $\boldsymbol{x}(s) = \begin{bmatrix} t(s) & K(s) \end{bmatrix}^T$ where $t(s)$ is time and $K(s) = \frac{v_x(s)^2}{2}$ is kinetic energy normalized by mass. Typically in predictive problems for HEVs, state of charge (SOC) is included as a state. For a BEV, the battery is the only energy source, so minimizing the power output of the motors will, in turn, reduce the power drawn from the battery. Therefore, SOC is not included in the state vector. The corresponding state dynamics are given by:

$$\dot{\boldsymbol{x}}(s) = \frac{d\boldsymbol{x}(s)}{ds} = \begin{bmatrix} \frac{1}{\sqrt{2K(s)}} \\ \dot{v}_x(s) \end{bmatrix} \tag{2.26}$$

where the longitudinal motion of the vehicle $\dot{v}_x(s)$ (assuming no lateral movement) is defined by:

$$\dot{v}_x(s) = \frac{1}{m_s}\left(F_x(s) - \rho_{air} A_f C_d K(s) - mgC_{rr}\cos\phi(s) - mg\sin\phi(s)\right) \tag{2.27}$$

where ρ_{air} represents air density, A_f frontal area, C_d the aerodynamic drag coefficient, g gravitational acceleration, C_{rr} the rolling resistance coefficient, $\phi(s)$ the road slope angle, and m_s the sum of vehicle mass m and equivalent mass of the rotating parts. The feasible set of the state vector, $\mathbb{X}$, is defined by the test case, and the feasible set of the control variables, $\mathbb{U}$, is defined by the capabilities of the motors and tires.

2.3.2 Instantaneous power optimization: control allocation

The task of the instantaneous optimization problem is to find the motor torque distribution that minimizes the power losses in the drivetrain, while fulfilling the demand on vehicle motion provided by a virtual driver or algorithm. To this end, control allocation is used. The optimization based control allocation problem in this thesis is formulated as,

$$\min_{\boldsymbol{T_m}} \quad P_{loss}\left(\boldsymbol{T_m}, \boldsymbol{\omega_m}\right) \tag{2.28a}$$

$$\text{s.t.} \quad \boldsymbol{v_{req}} = B\boldsymbol{T_m} \tag{2.28b}$$

$$\boldsymbol{T_m} \in \mathbb{U}_{\boldsymbol{T_m}} \tag{2.28c}$$

where $P_{loss}(\boldsymbol{T_m}, \boldsymbol{\omega_m})$ represents power loss expressions in terms of motor torque, $\boldsymbol{T_m}$, and motor rotational velocity, $\boldsymbol{\omega_m}$, $\mathbb{U}_{\boldsymbol{T_m}}$ represents the feasible set of the motor torques, and B is the control effectiveness matrix mapping the motor torques to the global force requests, $\boldsymbol{v_{req}}$[1],

$$\boldsymbol{v_{req}} = \begin{bmatrix} F_{x,req} \\ M_{z,req} \end{bmatrix} \tag{2.29}$$

where $F_{x,req}$ is the longitudinal force request, and $M_{z,req}$ is the direct yaw moment request. The direct yaw moment request is only applicable in the case of two motors on at least one axle. In the presence of a driver model, the longitudinal force request is derived from the

[1]Disclaimer: In Paper B, the motion request vector also includes lateral force, and the control vector incorporates the front wheel steering angle in addition to the motor torques. However, no clear conclusion could be drawn regarding the power benefit of this augmentation or the performance of its application. It is considered to be part of future work and is therefore left out here.

accelerator and brake pedal positions, multiplied by a factor to match driver-expected vehicle acceleration with pedal position. In contrast, the derivation of a direct yaw moment request is not as straight-forward since the yaw motion is not directly controlled by the driver, but is rather influenced by factors directly or indirectly related to vehicle characteristics (distance from center of gravity (CoG) to front and rear axle, height of CoG, anti-roll bar stiffness, etc.). Optimal direct yaw moment requests, with the objective to minimize tire losses, are explored in Paper C and detailed in Chapter 4. In all other cases, the yaw moment request is set to zero to avoid torque distributions that induce a yaw moment.

It is assumed that the actuator dynamics of the motors can be neglected. This is a common assumption in control allocation, and works as long as the closed-loop system is substantially slower than the actuator [9], which is applicable to the case here where the dynamics of the electric motor (the actuator) is significantly faster than the dynamics of the vehicle (the closed-loop system). One example where actuator dynamics cannot be neglected is in wheel slip control, as in anti-lock braking (ABS) and traction control (TC) systems. Another case is when the total control effort is shared between actuators with different dynamic responses, such as in a HEV combining a fast electric motor with a slower ICE. If the actuator dynamics are not considered, the delayed torque response from the ICE may cause the vehicle's initial motion to deviate from the desired behavior.

The output from the control allocator, $\boldsymbol{T}_{\boldsymbol{m}}^*$, is given by

$$\boldsymbol{T}_{\boldsymbol{m}}^* = \begin{bmatrix} T_{m,1}^* \\ \vdots \\ T_{m,p}^* \end{bmatrix} \tag{2.30}$$

where $T_{m,p}^*$ represents the power-optimal torque request of motor p, and p is the number of motors.

The two powertrain configurations considered in this thesis are presented in Figure 2.3. Powertrain configuration A shown in Figure 2.3a consists of four PMSMs, each individually connected to a wheel through a single-speed gearbox, a controllable coupling, and a stiff halfshaft. This configuration is used in Papers A, B and C. Powertrain configuration B in Figure 2.3b consists of a PMSM on the rear axle and an ASM on the front axle, connected to the wheels through a single-speed gearbox and an open differential, respectively. In this setup, the idle losses of the motors cannot be avoided by mechanically decoupling the PMSM and electrically switching off the ASM. This configuration is used in Paper D.

The PMSM is the most commonly used motor type in BEVs [56]. Besides its higher efficiency, it provides greater power density compared to the ASM, leading to smaller and lighter motor designs. However, PMSMs are significantly more expensive due to their reliance on rare earth metals for the magnets. A compromise can be made to offer good performance at a lower cost by using two different motor types in the powertrain, employed in vehicles such as the Tesla Model S [57]. In addition, the complementary characteristics of the two motors can improve the overall energy efficiency of the powertrain compared to configurations using two motors of the same type. While PMSMs typically have higher efficiency for most operating conditions, ASMs can be more efficient at high vehicle speeds. By assigning each motor to operate primarily within its respective high-efficiency region, the overall high-efficiency range of the powertrain is expanded.

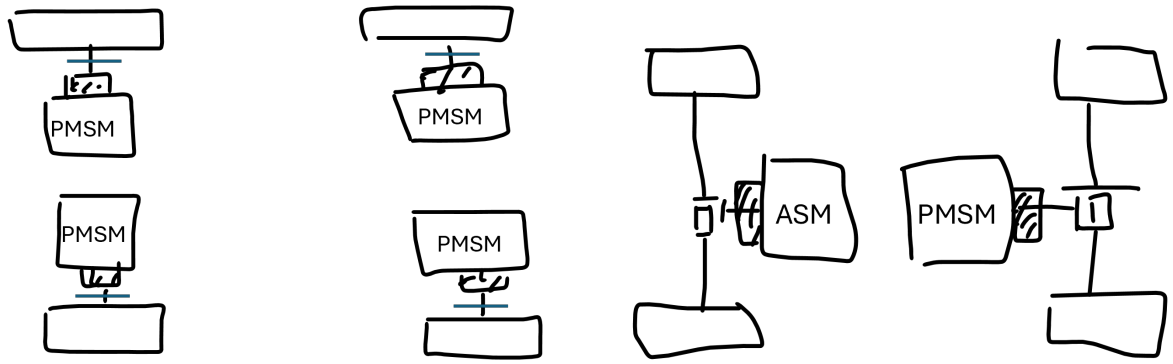

(a) *A: One PMSM per wheel (Papers A, B, and C).* **(b)** *B: Front axle ASM, rear axle PMSM (Paper D).*

Figure 2.3: *Two powertrain configurations, A and B, used in this thesis.*

Control Effectiveness Matrix, B

The linear relationship between the vehicle motion requests and the motor torques, i.e., the control effectiveness matrix B, is derived from a two-track vehicle model and the corresponding equations of motion for the longitudinal and yaw direction. The model is linearized through the small angle approximation, and only the dependence on motor torque is considered, resulting in the following relations,

$$F_{x,req} = \sum_{k=1}^{p} T_{m,k} \frac{n_k}{r_l} \tag{2.31}$$

$$M_{z,req} = \frac{w}{2r_l} \left(-T_{m,1} n_1 + T_{m,2} n_2 - T_{m,3} n_3 + T_{m,4} n_4\right) \tag{2.32}$$

where n_k represents the transmission ratio of motor $k \in \{1, ..., p\}$, r_l is the loaded tire radius, and w the vehicle track width. The control effectiveness matrix for the powertrain configuration including four PMSMs is formulated as,

$$B = \begin{bmatrix} \frac{n_1}{r_l} & \frac{n_2}{r_l} & \frac{n_3}{r_l} & \frac{n_4}{r_l} \\ -\frac{n_1 w}{2r_l} & \frac{n_2 w}{2r_l} & -\frac{n_3 w}{2r_l} & \frac{n_4 w}{2r_l} \end{bmatrix} \tag{2.33}$$

When the powertrain configuration consisting of one PMSM and one ASM is considered, the control effectiveness matrix is reduced to,

$$B = \begin{bmatrix} \frac{n_1}{r_l} & \frac{n_2}{r_l} \end{bmatrix} \tag{2.34}$$

The optimization problem defined in (2.28) is illustrated in Figure 2.4 for a longitudinal force request corresponding to a total motor torque of 80 Nm. The surface in the figure represents total power losses in the drivetrain, including both motor and tire losses, while the constraint line denotes all motor torque combinations that satisfy the total torque request. The optimal solution, comprising front and rear motor torques for powertrain configuration A, is given by $\boldsymbol{T}_{\boldsymbol{m}}^{*} = \begin{bmatrix} (T_{m,3} + T_{m,4}) & (T_{m,1} + T_{m,2}) \end{bmatrix}$ and is indicated by the blue dot. A magnified view is provided in Figure 2.4b, highlighting that $\boldsymbol{T}_{\boldsymbol{m}}^{*}$ corresponds to the point along the constraint line with the lowest total power loss.

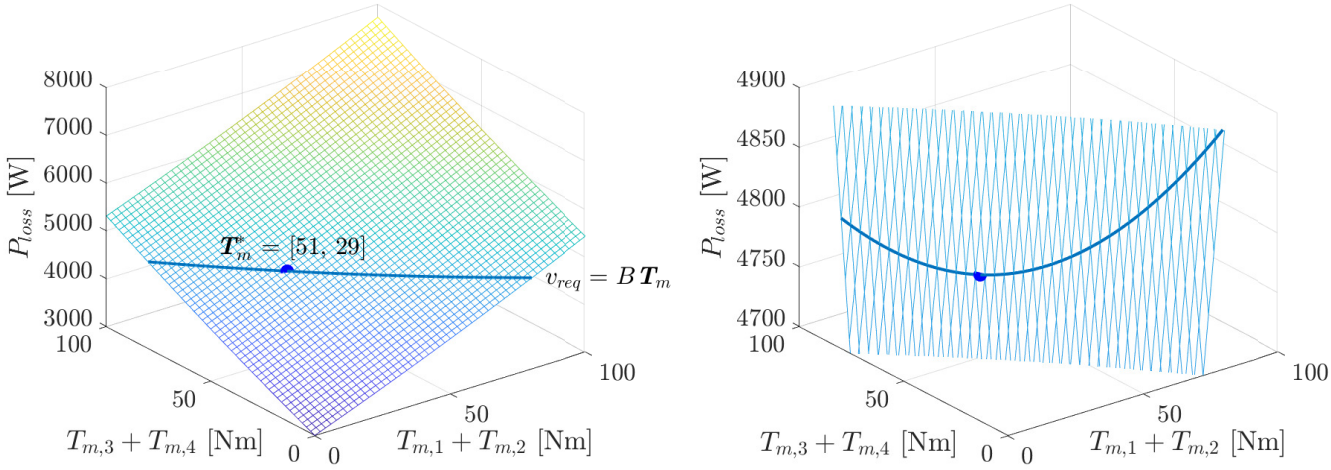

(a) *Full view.* **(b)** *Magnified view.*

Figure 2.4: *Illustration of the instantaneous optimization problem for* $v_{req} = 80$ *[Nm]* $\cdot\, n_{f/r}/r_w$*, considering powertrain configuration A where* $n_f = n_r$ *and the torque is shared equally within the axle. The line represents motor torque solutions fulfilling the motion request, and the dot corresponds to the optimal front and rear motor torque distribution.*

3

Energy consequences of a hierarchical function architecture

This chapter addresses the energy consequences of applying a hierarchical function architecture to the energy management problem, and explores how to enable such functional decomposition with minimal impact on energy consumption. The results are derived from Paper D.

3.1 Decoupling the energy management problem

The comprehensive EMP, including simultaneous optimization of velocity trajectory and motor torque distribution, is compared to a hierarchical approach, in which the optimization is decoupled in a predictive layer for the velocity trajectory, and an instantaneous layer for the torque distribution. Powertrain configuration B presented in Section 2.3.2 is considered, including an ASM on the front axle and a PMSM on the rear axle. Since the purpose is not real-time implementation but architecture concept evaluation, an optimal control problem is constructed and solved once for a road segment. The resulting control input is forwarded to a particle model that returns the energy consumption based on the motion of the particle and corresponding power losses in the motors.

3.1.1 Centralized and de-centralized architecture

The conceptual difference between the comprehensive and hierarchical EMP is illustrated in Figure 3.1. In the leftmost picture, the comprehensive EMP, or *centralized architecture* (CA) as it will be referred to in this thesis, is seen which optimizes the velocity trajectory and wheel torque distribution simultaneously in a predictive optimization framework. In the rightmost figure, the hierarchical function architecture, or *de-centralized architecture* (DCA) is illustrated optimizing velocity trajectory predictively, and motor torque distribution instantaneously.

In the OCP (2.22) of the predictive layer, the decoupling is realized by changing:

(1) The control variable vector, $\boldsymbol{u}(s)$.
In CA, the control variable vector includes the motor torques to be distributed, $\boldsymbol{u_{CA}} = [T_{mf}, T_{mr}]^T$, while in the decoupled problem DCA, the vector is reduced to $\boldsymbol{u_{DCA}} = [F_x]$.

(2) The objective function, $F_m(\boldsymbol{x}(s), \boldsymbol{u}(s))$.
The total force, $F_m(\boldsymbol{x}(s), \boldsymbol{u}(s))$, in the objective function is divided into two components,

$$F_m(\boldsymbol{x}(s), \boldsymbol{u}(s)) = F_x(\boldsymbol{x}(s), \boldsymbol{u}(s)) + F_{x,loss}(\boldsymbol{x}(s), \boldsymbol{u}(s)) \tag{3.1}$$

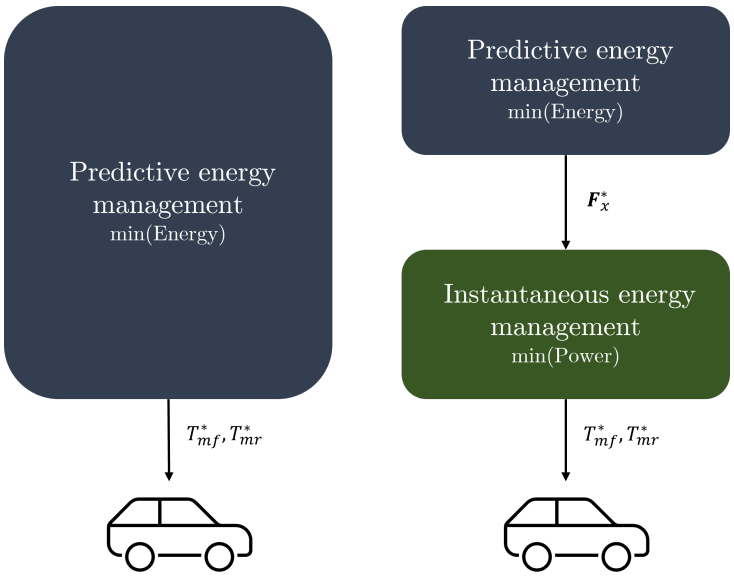

Figure 3.1: *Function architecture concepts: centralized architecture (left) and de-centralized architecture (right).*

where $F_x(\cdot)$ is longitudinal force required to move the vehicle generated by the electric motors, i.e., "useful" force, and $F_{x,loss}(\cdot)$ is the force equivalent to power that is lost in the motors. In CA, the objective function incorporates the power losses in the motors,

$$F^{CA}_{x,loss} = \frac{1}{v_x}\left(P_{loss,asm}(\omega_{mf}, T_{mf}) + P_{loss,pmsm}(\omega_{mr}, T_{mr})\right) \tag{3.2}$$

where $P_{loss,asm}$ and $P_{loss,pmsm}$ represent polynomial approximations of the power losses dependent on motor rotational speed and torque in ASM and PMSM, respectively. In DCA, the power losses in the motors are left out,

$$F^{DCA}_{x,loss} = 0 \tag{3.3}$$

The instantaneous layer of DCA incorporates the optimization problem (2.28) outlined in Section 2.3.2, with $\boldsymbol{T_m} = \begin{bmatrix} T_{mf} & T_{mr} \end{bmatrix}$, and $v_{req} = F^*_x$, where the vehicle motion request is the optimal longitudinal force F^*_x obtained from the predictive layer. Specifically, at each sample $k \in \{1, ..., N\}$, $v_{req}(k) = F^*_x(k)$, where N denotes the number of samples in the discretization. An alternative to vehicle motion control based on the optimal longitudinal force is to use the optimal velocity trajectory as the motion target. Implementing a feedback loop around this target velocity would enable the practical realization of the control architecture, as disturbances can cause deviations between the calculated and actual longitudinal force required to follow the velocity trajectory.

3.1.2 Refined de-centralized architecture

The hypothesis is that the potential energy consequences of excluding torque distribution from the predictive layer can be minimized if the predictive layer has some information on the combined powertrain efficiency. To this end, a refined version of the architecture concept DCA, referred to

as *refined de-centralized architecture* (r-DCA), is constructed where this information is provided in terms of an aggregated power loss map (APLM). The requirement on the APLM is that it should be a function of the optimization variables in DCA, as it should not introduce additional variables to the predictive layer. The force loss in (3.1) is reformulated accordingly,

$$F_{x,loss}^{rDCA} = \frac{1}{v_x}\left(P_{loss,APLM}(v_x, F_x)\right) \tag{3.4}$$

where $P_{loss,APLM}$ represents a polynomal approximation of the aggregated power loss map dependent on vehicle speed and longitudinal force.

Generation of the aggregated power loss map (APLM)

The APLM represents power losses of the entire powertrain, consisting of one or more electric motors, from the perspective of longitudinal vehicle operation, effectively serving as the equivalent of an electric motor's operational map but for the complete vehicle. It is defined by the total longitudinal force and forward velocity, F_x and v_x. The APLM exhibits infinite variability due to overactuation. In other words, for each operating point, defined by one combination of F_x and v_x, there are countless possible motor torque distributions, requiring a predefined allocation. To achieve the most power-efficient map, the torque distribution is optimized for each operating point to minimize power losses in the powertrain, and the corresponding losses are recorded. This means that the torque distribution could vary for different operating points in the APLM. The generation of the APLM is performed in the following way for the considered powertrain configuration:

1. Define the domain dictated by the capabilities of the combined powertrain: $F_x \in [F_{x,min}, F_{x,max}]$ and $v_x \in [0, v_{x,max}]$

$$F_{x,min} = \max\left(\frac{n_f}{r_l}T_{mf,min}, \mu F_{zf0}\right) + \max\left(\frac{n_r}{r_l}T_{mr,min}, \mu F_{zr0}\right)$$
$$F_{x,max} = \min\left(\frac{n_f}{r_l}T_{mf,max}, -\mu F_{zf0}\right) + \min\left(\frac{n_r}{r_l}T_{mr,max}, -\mu F_{zr0}\right)$$
$$v_{x,max} = \min\left(\frac{\omega_{f,max}}{n_f}, \frac{\omega_{r,max}}{n_r}\right) r_l$$

   where n_f and n_r represent the front and rear transmission ratios, $T_{mf,min}$ and $T_{mr,min}$ the lower operational torque limit on the front and rear motor, F_{zf0} and F_{zr0} the static normal load on the front and rear axle, $T_{mf,max}$ and $T_{mr,max}$ the upper operational torque limit on the front and rear motor, and $\omega_{f,max}$ and $\omega_{r,max}$ the maximum rotational speed for the front and rear motor, respectively.

2. Grid the domain into a number of operating points. Here:
   $N_{F_x} = 200$
   $N_{v_x} = 100$

3. Step through each operating point, find the optimal torque distribution through optimization and corresponding combined power losses.

   if: $F_x > (T_{mf,max}n_f + T_{mr,max}n_r)\frac{1}{r_l}$ or $F_x < (T_{mf,min}n_f + T_{mr,min}n_r)\frac{1}{r_l}$
   then: Force request exceeds powertrain capabilities. Return NaN.

else: (a) Find optimal torque distribution through the instantaneous optimization problem (2.28), here formulated as a non-linear program and solved using `fmincon` in Matlab.

(b) Use optimal torque distribution to find the combined powertrain losses through interpolation of raw power loss data[1] for the motors. Store power losses in a look-up table.

(c) Calculate the optimal combined powertrain efficiency, η. Store efficiency in a look-up table.

The power-optimal traction diagram, illustrating the efficiency contours of the APLM, is presented in Figure 3.2a, with the corresponding optimal torque distribution in Figure 3.2b. The traction diagram is only used for visualization, while a polynomial approximation of the APLM is used in the objective function of the OCP. The efficiency contours reveal that the powertrain is more efficient for low to medium longitudinal forces in the 15-40 m/s velocity range, and efficiency decreases dramatically for velocities below 15 m/s. The optimal torque distribution in Figure

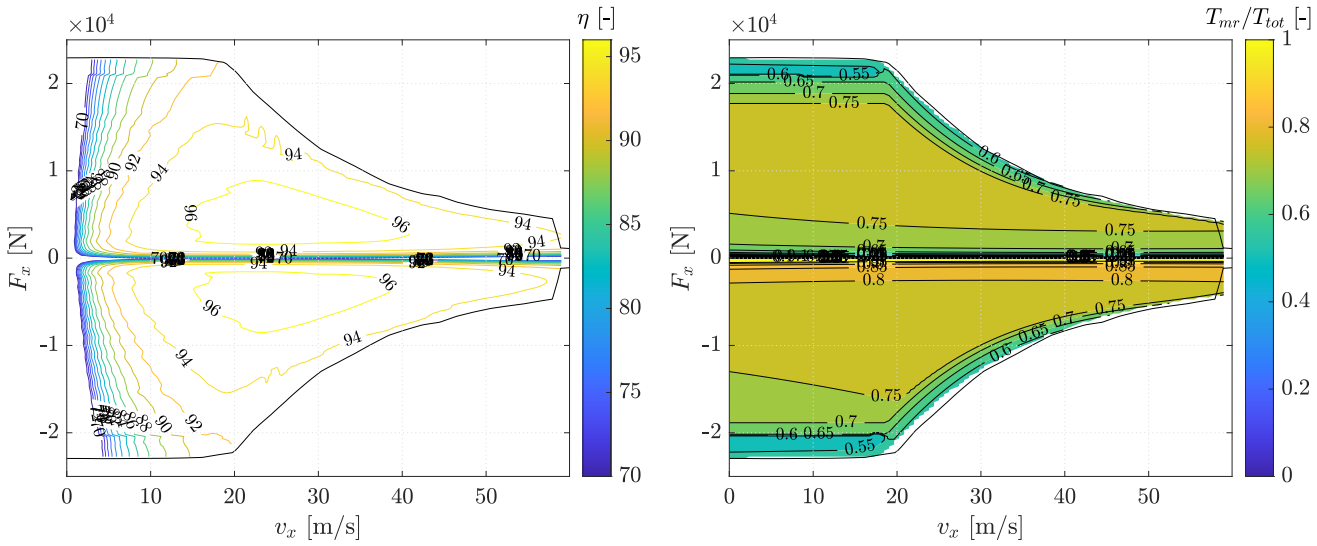

(a) *Power-optimal traction diagram with efficiency contours.* **(b)** *Power-optimal torque distribution,* T_{mr}/T_{tot}.

Figure 3.2: *Vehicle operational domain with powertrain optimal efficiency and torque distribution derived from APLM.*

3.2b is predominantly biased towards the rear motor (the PMSM) with 75% of the total torque request. At very high longitudinal force requests, the distribution is closer to equal between the motors.

[1]Raw power loss data refers to data acquired through simulation of high-fidelity motor models, or through experiments. In other words, it is not acquired using polynomial approximations, but rather using the data that constitutes the foundation for the polynomial approximations.

3.1.3 Case study

The case study includes a straight, 2500 m long road segment including a hill peaking in the middle of the segment. A minimum average velocity, $v_{avg,min}$, constrains the maximum travel time, t_f. Thus, the vehicle is allowed to cover the distance in less time than t_f. The velocity is liberally constrained, $v_x \in [1, 200]$ km/h, to fully explore what an energy-efficient velocity trajectory might look like. The initial and final velocity, v_0 and v_f, are set to be equal to $v_{avg,min}$. Different $v_{avg,min}$ and peak road grades are studied, with the purpose to target different operating regions and identify where electric vehicles could benefit from optimization of velocity trajectory when the powertrain efficiency is considered.

3.2 Decoupling effects on speed profile

The most energy-optimal[2] velocity trajectory is assumed to be provided by CA as it considers the motors' power losses individually in the OCP. The effects of decoupling the EMP are found by comparing the trajectory of CA to DCA, and the performance of the APLM is evaluated in terms of how closely the solution of r-DCA aligns with the solution of CA.

The velocity trajectories resulting from the three architectures are presented in Figure 3.3 for $v_{avg,min} = 15$ km/h and 5% peak road grade. The first notable observation is that CA and r-DCA produce similar sinusoidal-like velocity profiles that vary with topography, whereas DCA maintains a constant velocity equal to $v_{avg,min}$. This pattern holds for all scenarios considered in this work. The only resistance to be minimized in the OCP of DCA is the aerodynamic resistance, which increases quadratically with velocity. Consequently, the optimal solution is to maintain the lowest possible velocity within the given constraints. The velocity trajectories share a common initial and final velocity dictated by the boundary conditions in the OCP.

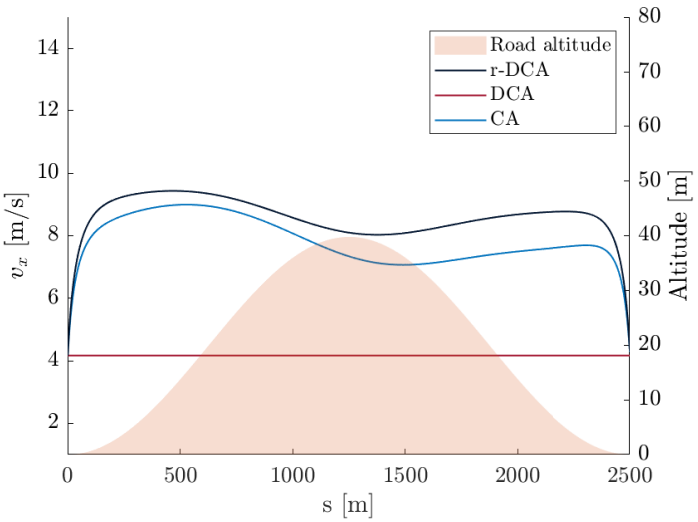

Figure 3.3: *Energy-optimal velocity trajectories of CA, DCA, and r-DCA for $v_{avg,min}$ =15 km/h and 5% peak road grade.*

[2]"most energy-optimal" is used as global optimality is not guaranteed due to the structure of the problem and the polynomial approximations of the power losses in the motors.

In the following sections, the dependence of the optimal velocity trajectory on $v_{avg,min}$ and peak road grade will be explored. As the velocity trajectories of CA and r-DCA consistently align closely, and DCA consistently produces velocity trajectories aligning with $v_{avg,min}$, the dependence will only be presented for CA here.

3.2.1 Dependence on minimum average velocity

The deviation of the energy-optimal velocity trajectory, provided by CA, from $v_{avg,min}$ is presented in Figure 3.4 for four different velocities. As can be observed, at $v_{avg,min} = 15$ km/h the optimal velocity deviates significantly from the minimum average. The velocity is initially increased, maintained at a higher average velocity with small variations due to topography, and then decreased to reach the final velocity. Studying $v_{avg,min} = 30, 50$ and 90 km/h, the same variation is observed due to topography, but the average velocity remains very close to the minimum average.

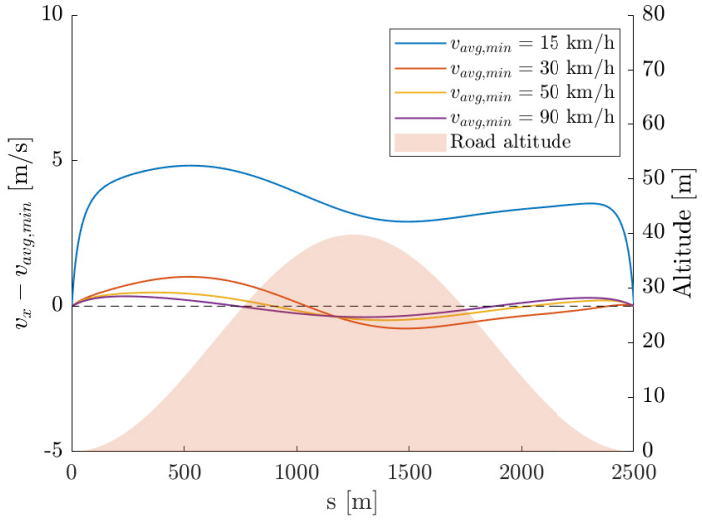

Figure 3.4: *Variation of optimal velocity trajectory, provided by CA, with respect to the minimum average velocity.*

The dependence on velocity can be explained by studying Figure 3.5, where the F_x-v_x trajectories are outlined in the power-optimal traction diagram. At $v_{avg,min} = 15$ km/h, presented in Figure 3.5a, the velocity trajectories of CA and r-DCA initially increase to enter more efficient regions of the powertrain, while DCA's solution maintains a constant velocity at lower powertrain efficiency.

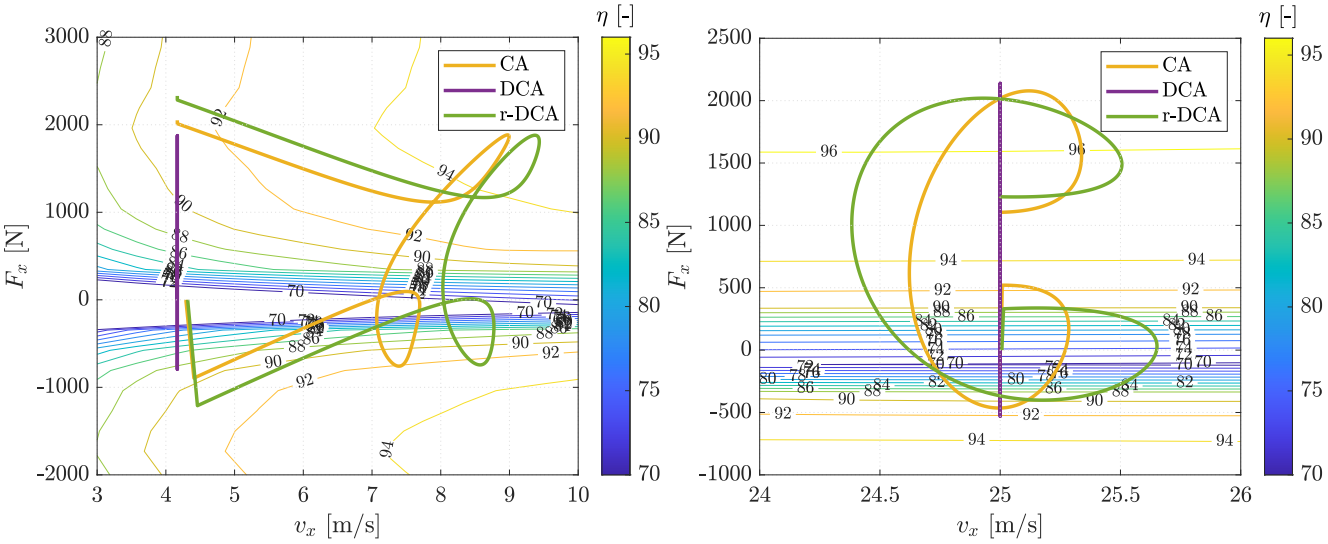

(a) $v_{avg,min} = 15$ *km/h.* **(b)** $v_{avg,min} = 90$ *km/h.*

Figure 3.5: *Solution trajectory in the power-optimal traction diagram for two minimum average velocities.*

CA and r-DCA should in theory provide the same optimal solutions since the polynomial approximations of the power losses used in the OCP of CA and in the generation of the APLM are the same. However, the power losses in the APLM is again fitted with a polynomial, $P_{loss,APLM}$, thereby being subject to another round of approximation errors. Studying the scenario with higher $v_{avg,min}$ in Figure 3.5b, it is not as clear that CA and r-DCA move into more efficient operating regions. It can be observed by studying the efficiency contours that the efficiency varies with longitudinal force and remains relatively constant with velocity, meaning there is little to be gained from increasing the velocity.

The power-efficient traction diagram is used here to help interpret the results, but it shows only powertrain efficiency. Important to note is that evaluating powertrain efficiency alone is insufficient as driving resistance, particularly aerodynamic drag, also increases with velocity. The energy consumption will only be reduced if the decrease in motor power losses is greater than the increase in driving resistance. The total energy consumption is considered in the OCP, and as will be shown in Section 3.3, employing CA and r-DCA lead to lower energy consumption compared to DCA.

3.2.2 Dependence on peak road grade

The effect of topography on the optimal velocity trajectory, provided by CA, is presented in Figure 3.6 at $v_{avg,min} = 15$ km/h for three peak road grades: 0, 5, and 10%. The hill illustration

in this figure is used to visually relate the velocity trajectory to the topographic shape, rather than to represent the actual altitude, which varies with the peak road grade. The initial increase in velocity remains, but the magnitude of the velocity variations grows as the peak road grade increases. The velocity reaches a higher value before the hill's peak, decreases at the top, and then rises again after passing the peak. Notably, the highest velocity occurs just before reaching the peak.

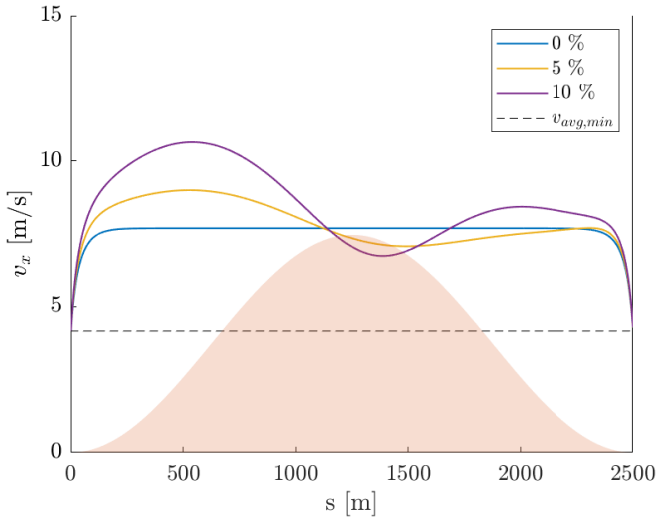

Figure 3.6: *Variation of optimal velocity trajectory, provided by CA, depending on peak road grade.*

For 0% peak road grade, the optimal velocity trajectory begins at the initial velocity, increases to and maintains a higher constant average velocity, and then decreases to the final velocity. However, in [41], the constant velocity phase is dictated by pulse and glide (PnG) at a high frequency, which is not seen here. The PnG behavior is also supported by [43, 58]. In the literature mentioned, the assumption is that the powertrain energy consumption is negligible in the PnG glide phase, i.e., there are zero power losses at zero torque, which could explain PnG as it is "free" in terms of energy to not apply any torque. However, the idle losses at zero torque have a significant impact on the energy consumption and resulting optimal torque distribution. If a mechanical disconnect from the wheels in case of PMSM, or electrical switch off in case of ASM, is incorporated with no cost related to the coupling/decoupling event, it is possible that the PnG-behavior could be seen here as well.

The dependence on road grade can be understood by studying the power-optimal traction diagram, presented in Figure 3.7, for 0, 5 and 10% peak road grade, respectively.

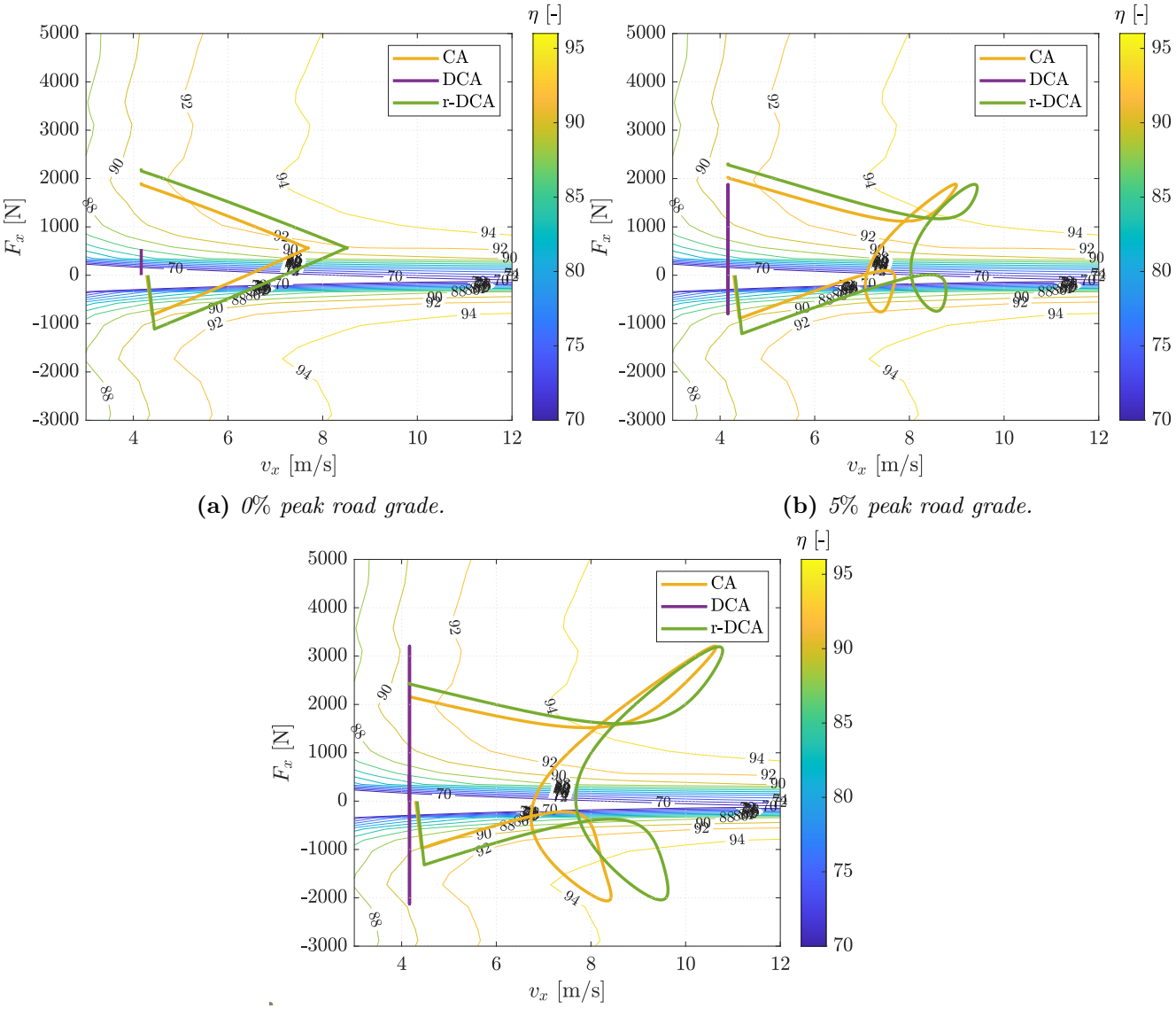

(a) *0% peak road grade.*

(b) *5% peak road grade.*

(c) *10% peak road grade.*

Figure 3.7: *Solution trajectory in the power-optimal traction diagram for three peak road grades.*

With an increase in peak road grade, the longitudinal force demand increases to overcome grade resistance. As the longitudinal force demand increases, the operating region extends into more efficient areas of the powertrain. This can be observed by studying Figures 3.7a, 3.7b, and 3.7c sequentially, where the solution trajectories shift further into higher-efficiency regions with increasing peak road grade.

3.2.3 Real world driving cycle: Artemis Urban Cycle (AUC)

In the previous scenarios, the velocity was loosely constrained, except for the initial and final velocities. Although this flexible test setup is useful for exploring energy-efficient velocity profiles, the resulting dynamic profile, for example increasing the speed in the low-speed scenario, is

rarely feasible in practice. An additional driving scenario is required to evaluate the decoupling effects in more realistic situations. To this end, the Artemis urban cycle (AUC) is used. The velocity profile defined by this drive cycle serves as the reference velocity, v_{ref}, and the solution is allowed to deviate by up to 10% from it,

$$0.9 \cdot v_{ref} \leq v_x \leq 1.1 \cdot v_{ref} \tag{3.5}$$

Furthermore, the lower bound on the velocity is constrained to 10 km/h as the OCP in current design is not able to handle velocities reaching 0, as in the original AUC.

The velocity profiles of CA, DCA and r-DCA are presented in Figure 3.8 along with the reference velocity. The velocity profile of DCA closely follows the lower velocity limit throughout the

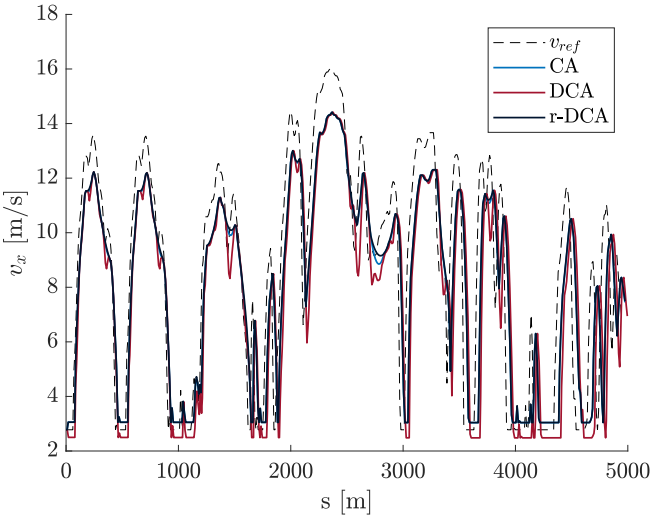

Figure 3.8: *Velocity profiles for Artemis urban drive cycle: reference, CA, DCA, and r-DCA.*

drive cycle, consistent with the behavior observed in previous driving scenarios. As before, CA and r-DCA exhibit similar velocity profiles, here avoiding rapid variations and aligning with the upper velocity limit when the reference velocity is low.

3.3 Effects on energy consumption

The energy consumption at different velocities is summarized in Table 3.1. The energy consequences of decoupling the EMP are more pronounced at lower velocities, which is expected due to the substantial differences in velocity profiles between CA and DCA. At $v_{avg,min} = 15$ km/h, using DCA results in a 3.5% increase in energy consumption compared to CA. However, by incorporating the APLM into the objective function of the OCP, the r-DCA approach reduces this increase to 0.4%. For medium to high velocities (30–90 km/h), the impact of decoupling on energy consumption is minimal, with DCA resulting in only a 0.1–0.2% increase in consumption relative to CA. For the real-world driving cycle (AUC), DCA consumes 2.2% more energy than CA, r-DCA achieves approximately the same energy efficiency as CA, and following the velocity profile of AUC, $v_x = v_{ref}$, increases the energy consumption by 4.2%.

Table 3.1: *Energy consumption of CA, DCA and r-DCA for different $v_{avg,min}$. The presented cases with a constant $v_{avg,min}$ incorporate 5% peak road grade, whereas AUC assumes 0%. Positive numbers indicate an increase in energy consumption.*

$v_{avg,min}$ [km/h]	Strategy	E [kWh]	ΔE
15	CA	0.4380	ref
	DCA	0.4532	3.5%
	r-DCA	0.4398	0.4%
30	CA	0.4382	ref
	DCA	0.4389	0.2%
	r-DCA	0.439	0.2%
50	CA	0.4661	ref
	DCA	0.4665	0.1%
	r-DCA	0.4661	0.0%
90	CA	0.5953	ref
	DCA	0.5958	0.1%
	r-DCA	0.5950	-0.1%
v_{ref} = AUC	CA	0.9275	ref
	$v_x = v_{ref}$	0.9668	4.2%
	DCA	0.9482	2.2%
	r-DCA	0.9276	0.0%

Notably, the reductions in energy consumption of r-DCA, along with the velocity profile previously presented, closely align with those of CA. To reduce the energy consumption at $v_{avg,min} = 15$ km/h, the velocity must increase by 4-5 m/s which is approximately twice the initial and final speed in this case. Such an increase might not be acceptable in realistic low-speed scenarios, e.g., city driving. However, the results using AUC show that by imposing stricter limits on the allowed velocity deviation, significant energy savings are still possible, even though the cycle also includes higher velocity segments where the decoupling effects are not as pronounced.

An evaluation of the energy consequences for different peak road grades, as presented in Table 3.2, shows that the energy consequences of DCA increase with higher peak road grades when

compared to CA. For a flat road (0% peak grade) at $v_{avg,min}$ = 15 km/h, DCA results in a 1.7% increase in energy consumption. As the peak road grade increases to 10%, the energy consumption rises significantly, reaching a 8.2% increase. However, these energy consequences can be effectively mitigated by using r-DCA. With the APLM incorporated into the objective function, the increase in energy consumption is reduced to just 0.4% at 0% peak road grade and 0.2% at 10% peak road grade.

Table 3.2: *Energy consumption of CA, DCA and r-DCA for different peak road grades. The presented cases incorporate $v_{avg,min}$ =15 km/h.*

Peak road grade [%]	Strategy	E [kWh]	ΔE_{DCA}
0	CA	0.4269	ref
	DCA	0.4343	1.7%
	r-DCA	0.4287	0.4%
5	CA	0.4380	ref
	DCA	0.4532	3.5%
	r-DCA	0.4398	0.4%
10	CA	0.4640	ref
	DCA	0.5019	8.2%
	r-DCA	0.4648	0.2%

3.4 Optimality of results

The optimization problems considered in all three architectures, both the OCPs and the instantaneous formulation, are non-convex due to non-convexity of the motor power loss polynomials and control variable constraints and the non-linear dynamics. Therefore, global optimality cannot be guaranteed. However, the confidence in the solutions being globally optimal is increased by applying perturbations using multiple initial guesses and assessing if the resulting optimal solution remains unchanged. Eight initial guesses were assessed: four consisted of variations in velocity trajectory and the remaining four of variations in torque distribution. The initial guesses were designed to approach the optimal solution from the top and from the bottom. All solutions converged to the optimal solutions for each architecture, respectively.

3.5 Key findings

To summarize this chapter, the following key findings are identified:

- The energy-optimal velocity trajectory reaches a higher average velocity at low minimum average velocities, and aligns closely with the minimum average velocity at high velocities.
- The energy consequences of decoupling the EMP results in an increase in energy consumption ranging from 0.1% to 8.2%, where the consequences are more pronounced at lower velocities and higher peak road grades.
- The solutions of r-DCA closely align with those of CA, both in terms of velocity profile and

energy consumption. Thus, a hierarchical function decomposition of the EMP is enabled, in terms of minimal energy consequences, by augmenting the objective function of the OCP with an aggregated power loss map.

- The aggregated power loss map, defined in terms of vehicle longitudinal force and forward velocity, is generated using the power-optimal torque distribution.

4

Power-optimal torque distribution

To minimize power consumption through motor torque distribution, one must consider the actuating components responsible for generating vehicle motion. Some components have a greater impact on energy consumption due to higher power losses and/or greater sensitivity to torque distribution. This chapter analyzes the individual influence of four key actuating components: the electric motors, couplings, transmission, and tires. The findings are based on results from Papers A, B, and C.

4.1 Instantaneous optimization methods

The instantaneous optimization methods applied to the problem of power-optimal wheel torque distribution incorporate online and offline optimization, namely quadratic programming and brute force optimization. Both methods are selected and designed for real-time applicability, calling for fast and efficient solutions. In the research presented in this part of the thesis, powertrain configuration A presented in Figure 2.3a is considered, incorporating four identical PMSMs.

4.1.1 Online method: Quadratic program

The quadratic program (QP) is selected for online optimization due to its convex properties provided a convex set of constraints, thereby ensuring global optimality of the solution. In addition, the solution can be obtained analytically if the saturation limits of the actuators are neglected, further increasing the computational speed. The optimization problem (2.28) is formulated as a quadratic program according to,

$$\min_{\boldsymbol{T_m}} \quad \frac{1}{2}\boldsymbol{T_m}^T Q(\omega_m)\boldsymbol{T_m} + f(\omega_m)^T\boldsymbol{T_m} \tag{4.1a}$$

$$\text{s.t.} \quad \boldsymbol{v_{req}} = B\boldsymbol{T_m} \tag{4.1b}$$

The power losses are expressed as quadratic functions of the control variables, i.e., the motor torques $\boldsymbol{T_m}$, where the first coefficient of the polynomial is stored in $Q(\omega_m)$ and the second coefficient of the polynomial stored in $f(\omega_m)$. Since the power losses are also dependent on motor rotational velocity, in addition to motor torque, multiple polynomials are approximated at different motor speeds, here reflected in Q's and f's dependence on ω_m. In the control architecture, the velocity of the motors is evaluated prior to the control allocator, and a suitable polynomial is selected to be used in the QP. By introducing Lagrangian multipliers, $\boldsymbol{\lambda}$, the

original optimization problem (4.1a) is relaxed according to,

$$\min_{\boldsymbol{T_m},\boldsymbol{\lambda}} \quad \frac{1}{2}\boldsymbol{T_m}^T Q(\omega_m)\boldsymbol{T_m} + f(\omega_m)^T\boldsymbol{T_m} + \boldsymbol{\lambda}^T\left(B\boldsymbol{T_m} - \boldsymbol{v_{req}}\right) \tag{4.2a}$$

where $\boldsymbol{\lambda}$ is a diagonal, symmetric matrix with the same dimension as the number of elements in $\boldsymbol{v_{req}}$. The unconstrained problem can be solved analytically through,

$$\begin{bmatrix}\boldsymbol{T_m^*}\\ \boldsymbol{\lambda}\end{bmatrix} = \begin{bmatrix}Q(\omega_m) & B^T\\ B & \mathbf{0}\end{bmatrix}^{-1}\begin{bmatrix}-f(\omega_m)\\ \boldsymbol{v_{req}}\end{bmatrix} \tag{4.3}$$

The full derivation is given in Appendix C. There are numerous ways to handle actuator saturation in the control allocation problem, namely, through direct allocation, daisy chaining, and redistributed pseudoinverse among others [9, 10]. The simplest way to incorporate constraints is to truncate by limiting the controls that violate some constraints and redistributing the difference to the remaining control inputs, an approach adopted in this work. In online or offline optimization, actuator saturation can be easily implemented in the problem formulation. However, considering real-time application, simpler problem formulations are needed to ensure fast computation and convergence. The methods often involve analytical solutions, distribution rules or lookup tables dependent on total torque demand and forward velocity. Some of these methods, e.g., analytical expressions of the optimal solution, require limitations on the control variables to be neglected. The authors in [21, 22] limit the torque requests afterwards, and redistributes remaining torque to unsaturated actuators while still fulfilling the motion requests. In [17], it seems that, although not explicitly stated, the actuator limits are simply neglected. This rarely becomes an issue, as moderate driving is most often considered and even distribution is optimal for high torque demands, which ensures that the torque demands are relatively low and actuators are further from their limits. One situation where it could become problematic when the road-tire friction is low as the torque is commonly also limited by available tire friction force. However, during these road conditions, stability should be prioritized over energy efficiency.

Coupling management strategy

To include a coupling, a QP-based algorithm is designed incorporating three separate QPs representing different motor utilization strategies: QP FWD, QP RWD, and QP AWD. As the names suggest, QP FWD considers the front motors coupled and rear motors decoupled, QP RWD considers the front motors decoupled and rear motors coupled, and QP AWD considers the front and rear motors coupled. The algorithm is illustrated in Figure 4.1. The motion request, $\boldsymbol{v_{req}}$[1] is forwarded to each QP, which returns the optimal motor torque distribution and corresponding power losses. Then, a final layer chooses the torque distribution that provides the minimal power losses and forwards the motor requests to the actuator control in the vehicle.

[1] In Paper A, a total motor torque request, $T^{tot}_{m,req}$, is used instead of longitudinal force request, $F_{x,req}$, since the motors share the same transmission ratio. In Paper B, where the transmission ratio varies between the front and rear motors, this is less suitable as the total motor torque request depends on how the torque is distributed.

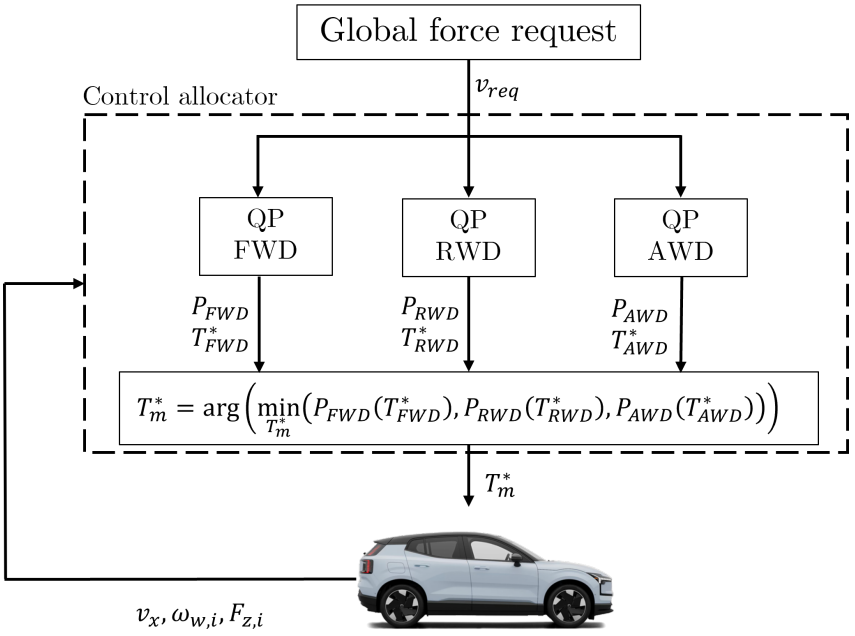

Figure 4.1: *Coupling management strategy of the QP-based algorithm.*

4.1.2 Offline method: Brute force approach

The brute force approach is an intuitive method in which all possible candidate solutions to a problem are evaluated, and the best one is chosen. It is rarely used as a real-time method as it is computationally demanding, rather as a benchmark for online optimization methods and/or as a foundation for control rules and lookup tables.

In this work, for example, the brute force method is used to generate a lookup table (LUT) offline for the power-optimal motor torque distribution dependent on longitudinal force request $F_{x,req}$ and velocity, v_x,

$$\boldsymbol{T}^*_{\boldsymbol{m}} = \mathrm{LUT}(F_{x,req}, v_x) \tag{4.4}$$

The LUT is then implemented online in simulation. To simplify the LUT, dependencies on, e.g., vertical load are not included; rather, the static vertical load is used. Furthermore, the LUT is limited to the longitudinal dimension, i.e., it does not include direct yaw moment requests, $M_{z,req}$. The generation of the LUT is relatively straightforward: the total power losses (motor and longitudinal tire losses) of different coupled/decoupled motor combinations are analyzed using the brute force approach, selecting the best combination and torque distribution to be stored at each operating point of the discretized vehicle operational domain. It is important to note that the lookup table is specific for the transmission ratios used during its generation. Apart from being used as a method to distribute torque optimally, the LUT is also used as a benchmark to evaluate the performance of the QP, considering the quadratic approximations of the power losses in the motors. The results obtained by using the LUT and QP consistently agree, with minor differences, as demonstrated in Paper A. Therefore, a detailed comparison of the two methods is not included here. The results presented in the remainder of this chapter are derived from the two methods interchangeably, either selected arbitrarily or based on which method was used to analyze the specific point of interest.

4.2 Decoupling the motors from the wheels

The motor type considered in powertrain configuration A, the PMSM, has significant idle losses mainly caused by a permanent magnetic field rotating with the motor. By introducing a coupling that mechanically disconnects the motors from the wheels, the idle losses can be avoided by stopping the rotation, leading to further reductions in energy consumption. In fact, using identical PMSMs, within the context of power-optimal torque distribution, it will be shown that the ability to decouple the motors is by far the most significant contributor to energy savings.

4.2.1 Effects on torque distribution

The effect of including a coupling on the optimal motor torque distribution can be seen in Figure 4.2, where the front-to-total torque distribution for positive total motor torque requests at three rotational motor velocities is presented with and without couplings.

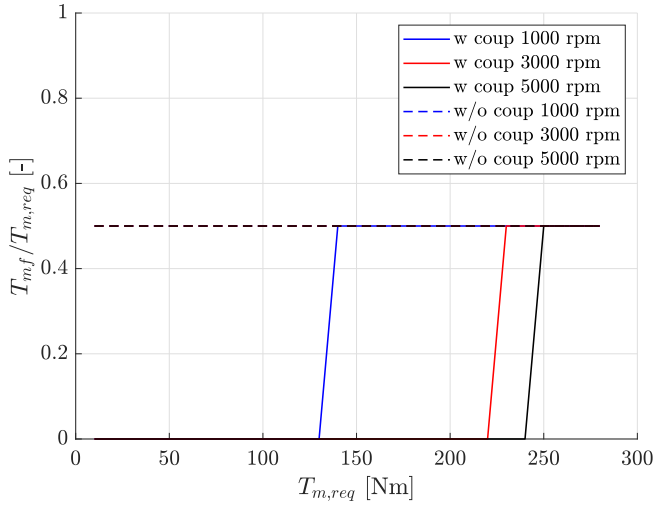

Figure 4.2: *Optimal front to total torque distribution with and without couplings for three motor rotational velocities, derived using QP.*

In the absence of couplings, equal torque distribution between the motors (if identical and PMSM) is optimal in terms of energy (supported by [12, 13]). This is to be expected, as the power losses are quadratic in nature and the motors are identical. To minimize power losses in this case, the torque on each motor should be as low as possible. When couplings are involved, however, the distribution includes two operating modes of the powertrain: single-axle and equal torque distribution. The single-axle mode is favorable up until a torque threshold where the distribution changes to equal torque between the motors. The threshold at which total torque request is redistributed increases with rotational velocity. These two modes are also found in [14]. To clearly illustrate the effect of couplings, only motor losses are considered in Figure 4.2, as these are specifically targeted by the couplings.

The consequent distribution of motor torque during driving is presented in Figure 4.3 for a finite segment of GCC, where decoupled motors are represented by zero torque.

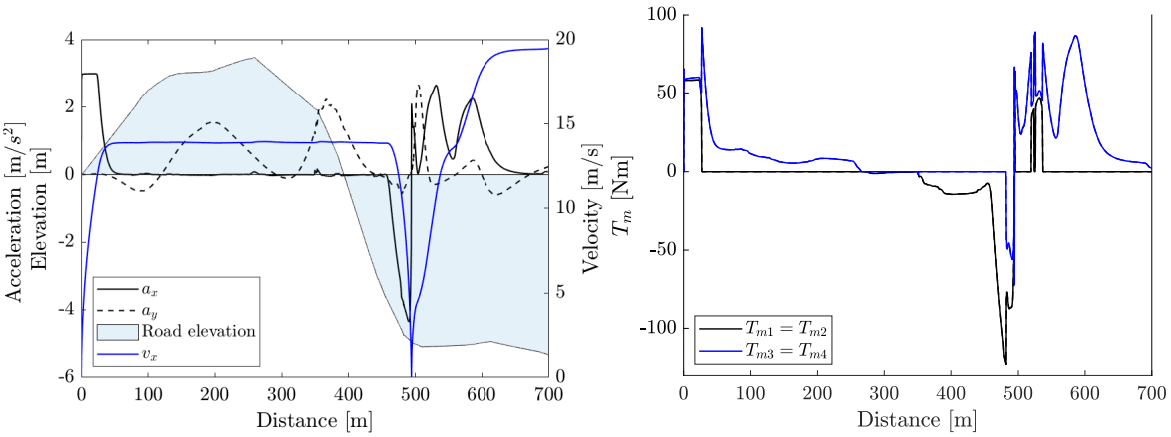

(a) *Vehicle states and road elevation.* **(b)** *Optimal torque distribution (QP)*

Figure 4.3: *Optimal torque distribution (QP) with couplings and vehicle states for a limited segment of GCC.*

An acceleration event takes place at the very beginning of the segment, 0 - 30 m, where all four motors are used since the velocity is relatively low and the torque demand is high. As the velocity increases, torque is redistributed to single-axle propulsion. Between 450-550 m, the vehicle is decelerated to a standstill, and then accelerates again.

In Figure 4.3, the complete drivetrain losses are considered, including tire losses as well. Consequently, the distribution and torque threshold changes, which can be depicted in Figure 4.3 by, e.g, the unequal torque distribution when both motors are used, and the selection of the front axle for propulsion and rear axle for braking at low torque demands. The effect of including tire losses in the objective function on torque distribution and energy consumption is further discussed in Section 4.4.

4.2.2 Effects on energy consumption

The energy consumption is evaluated using the Gothenburg City Cycle (GCC), which reflects everyday driving. Table 4.1 presents the results for three torque distribution strategies: equal distribution (ED) as a reference, the QP-based algorithm with couplings, and the same QP optimization without the ability to decouple the motors. Compared to ED, the QP with couplings reduces energy consumption by 3.9%. Without couplings, the reduction diminishes to 0.2%. Since the optimal torque distribution considering only motor losses results in equal distribution, as discussed in the previous section, the marginal improvement indicates that the main contributor to energy savings with four identical PMSMs is the use of couplings and their control algorithm.

Table 4.1: *Energy consumption GCC: the effect of couplings.*

Strategy	E_{cons} [Wh/km]	ΔE_{cons}
ED	184.4	ref
QP w. coupling	177.2	-3.9%
QP w.o. coupling	184.0	-0.2%

4.3 Single-speed transmission ratio

The transmission ratio affects the operating region of the electric motors, as the power demand is determined on a vehicular level. Figure 4.4 presents the traction diagram for PMSM 2 with two different transmission ratios. The trade-off between maximum longitudinal force and velocity, $F_{x,max}$ and $v_{x,max}$, can be observed by comparing Figures 4.4a and 4.4b. A lower transmission ratio, presented in Figure 4.4a, leads to lower $F_{x,max}$ and higher $v_{x,max}$. The opposite is true for a higher transmission ratio, as can be seen in Figure 4.4b. In addition, changing the transmission

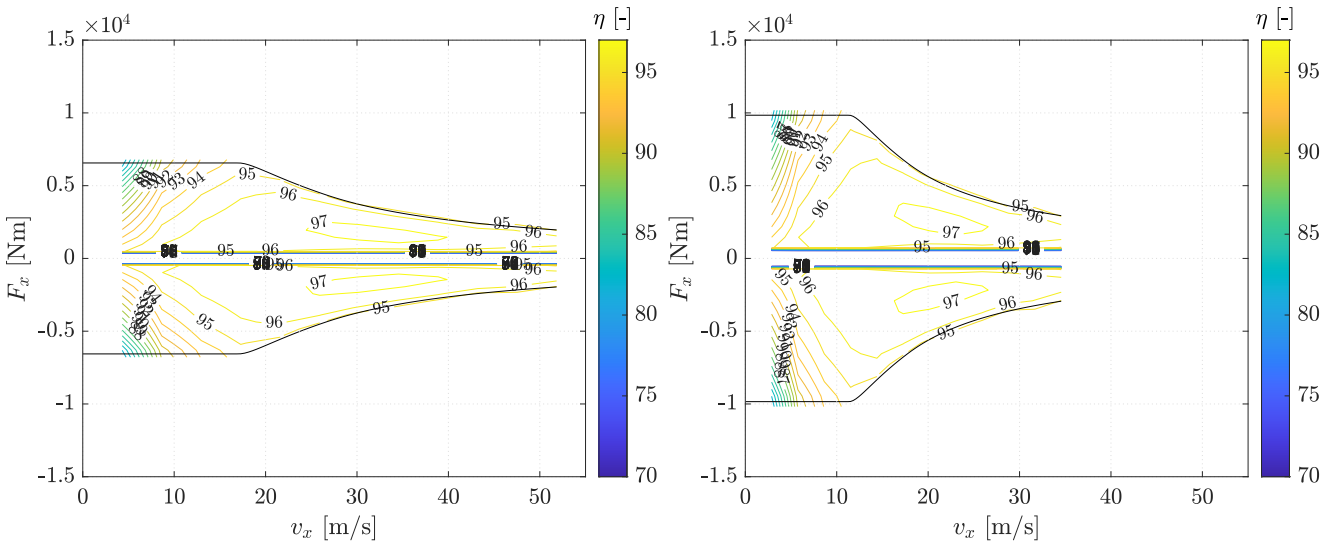

(a) $n = 8$. **(b)** $n = 12$

Figure 4.4: *Traction diagram of PMSM 2 with efficiency contours for two transmission ratios, n.*

ratio leads to different optimal operating regions of the traction diagram: with a lower ratio the high-efficiency region is shifted to high-velocity and low-torque regions, whereas with a higher ratio it is shifted to low-velocity and high-torque regions. By optimizing the transmission ratio, particularly in combination with the optimization of motor torque distribution, the strategies can reinforce each other, leading to lower energy consumption than if each were applied independently.

4.3.1 Energy-optimal front-to-rear transmission ratio

The transmission ratio is defined at the axle level, which means that both motors driving the same axle share the same ratio. The exploration space is defined as $n \in \{6, 14\}$, where the energy-optimal front-to-rear transmission ratio combination, $(n_f/n_r)^*$, is found using the brute force approach. Specifically, for each (n_f/n_r), GCC is simulated using the QP-based algorithm

described in Section 4.1.1, and the corresponding energy consumption is recorded. The energy-optimal $(n_f/n_r)^*$ is identified as the combination that yields the lowest energy consumption. The gear efficiency is assumed to be the same for all ratios.

The resulting $(n_f/n_r)^*$ incorporates different ratios on the front and rear axle, $n_f = 14$ and $n_r = 8$. The order is specific, i.e., it is not as energy efficient with $n_f = 8$ and $n_r = 14$, as it is dictated by tire power losses which depend on vertical axle load (discussed further in Section 4.4). It is important to note that the optimal front-to-rear transmission ratio is dependent on the power demand of the analyzed drive cycle and driver model, as it determines the operating regions most frequently visited in the motor efficiency maps. Therefore, the results may vary depending on whether urban or highway driving is considered. The drive cycle used here, GCC, includes both, possibly leading to a suboptimal transmission ratio combination considering each scenario independently, but a better one considering both.

4.3.2 Effects on torque distribution

The concept of different gear ratios on the front and rear axle is similar to the cruise and startability electric axle concept described in [59] for heavy vehicles. Simply put, the key idea is that one axle is dimensioned for high velocities and low torque demands and the other axle for low velocities and high torque demands. Studying the resulting torque distribution using $(n_f/n_r)^*_{QP}$ found in combination with the QP algorithm, presented in Figure 4.5 for the same road segment given in Figure 4.3a, the startability/cruise axle concept can be observed.

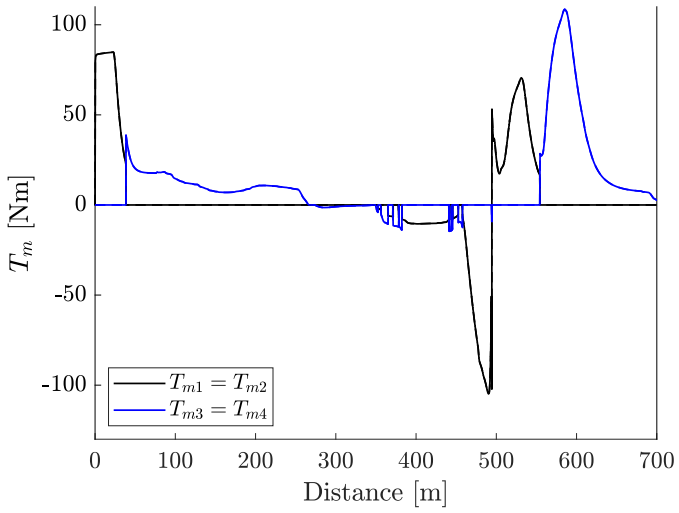

Figure 4.5: *Optimal torque distribution with optimal front-to-rear gear ratio:* $n_f = 14$, $n_r = 8$.

In the beginning of the segment, at 0 - 50 m, only the front axle is used which has the higher transmission ratio. A higher transmission ratio results in lower torque demands on the motor to meet the longitudinal force request. Consequently, as the rotational velocity of the motors increase with a higher transmission ratio, the increase in power losses eventually leads to a decoupling event of the front motors at approximately 50 m, and the rear motors provide the demanded torque. This behavior is consistent throughout the presented road segment, where the

front motors are used mainly during low speed, and the rear motors are used during high speed. The oscillation between the front and rear motors indicates the presence of a transition point, where the power losses of the two distributions are similar. Such oscillatory behavior needs to be avoided as it will be costly, both in terms of the coupling/decoupling event and comfort.

4.3.3 Effects on energy consumption

The energy consumption of the QP-based algorithm with corresponding $(n_f/n_r)^*_{QP}$ is again compared to ED with its respective $(n_f/n_r)^*_{ED}$. The optimal front-to-rear gear ratio for ED is the same on the front and rear axle, $n_f = n_r = 12$. This can be explained by the quadratic nature of the electric losses, where it is optimal to distribute the torque equally among the *motors*. Since ED concerns an equal *wheel* torque distribution, an equal *motor* torque distribution occurs only when the same transmission ratio is used on the front and rear axle.

Studying the energy consumption in Table 4.2, there is a clear benefit of optimizing front-to-rear transmission ratio in combination with torque allocation algorithms. Using $(n_f/n_r)^*_{ED}$ and optimizing the torque distribution with the QP algorithm, the energy consumption is reduced by 6%. Using $(n_f/n_r)^*_{QP}$, the energy consumption is reduced by 8.4%, meaning that the energy benefit of the joint optimization of front-to-rear transmission ratio and torque distribution is 2.4%-units.

Table 4.2: *Energy consumption GCC: the effect of transmission ratio.*

Strategy	$(n_f/n_r)^*$	E_{cons} [Wh/km]	ΔE_{cons}
ED	12/12	183.7	ref
QP w. coupling	12/12	172.7	-6.0%
QP w. coupling	14/8	168.3	-8.4%

4.4 Minimizing tire power losses

Motor torque and steering angles are ultimately translated into longitudinal and lateral forces through the tires. In this translation, power is lost due to rolling resistance, longitudinal slip, and lateral slip, which can be minimized through deliberate torque distribution. This section aims to assess the magnitude of tire power loss minimization through torque distribution on energy consumption. It is divided into longitudinal and lateral tire losses.

4.4.1 Front-to-rear torque distribution: longitudinal tire losses

The longitudinal tire losses consist of longitudinal tire slip and rolling resistance. The longitudinal tire and electric energy losses in GCC is presented in Figure 4.6 for three fixed torque distributions: FWD with rear axle decoupled, RWD with front axle decoupled, and ED, and three torque distribution strategies: equal friction utilization (EFU), LUT and QP. EFU is designed to distribute torque such that the tire work load is equal on all tires, i.e., the ratio between the longitudinal force and friction force capability, determined by tire-road friction and normal load, is the same.

As can be observed, the rolling resistance is the most prominent energy loss. In fact, rolling resistance accounts for approximately 18-25% of the total required traction energy in a ICEV [60]. However, there are minor differences between the torque distribution strategies. The main component of rolling resistance is dependent on vertical load and velocity, leaving only a small component affected by the torque distribution.

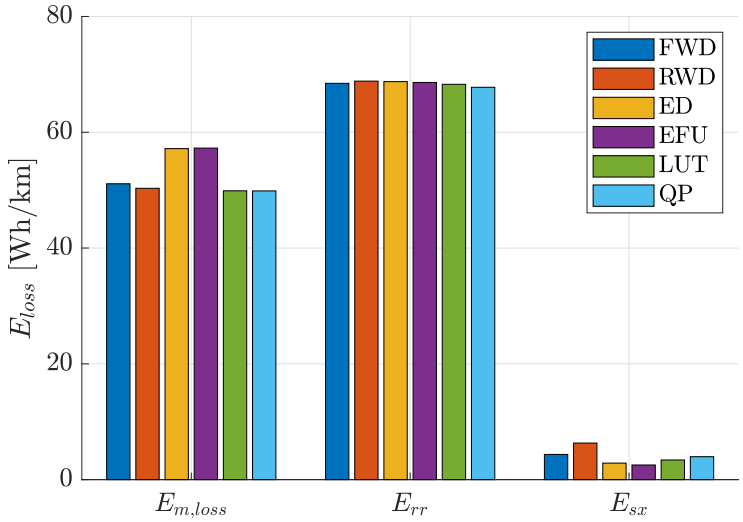

Figure 4.6: *Electric ($E_{m,loss}$), rolling resistance (E_{rr}) and longitudinal tire slip (E_{sx}) energy losses for GCC (Paper A).*

The longitudinal tire slip losses are significantly smaller but depend to a higher extent on the torque distribution as shown in Figure 4.6. The highest slip losses are observed for FWD and RWD, as these predominantly distribute torque to one axle. The vehicle considered has higher normal load on the front axle, leading to the highest slip losses in RWD as the rear axle experience greater slip. Since the slip losses are quadratically dependent on slip (see (2.12)), EFU exhibit the lowest losses, as evenly distributing the work load leads to equal slip for the tires.

The effect of tire losses on the optimal torque distribution can be assessed by comparing Figure 4.2 to Figure 4.7. The greatest difference is seen when no couplings are considered, where the single-axle mode is still preferred at low torque demands. The distribution is biased towards the rear axle, which experiences a lower normal load compared to the front axle. This can feel contradictory considering slip losses, as they are reduced with higher longitudinal tire stiffness resulting from a higher normal load. However, there is a trade-off between the modeled P_{rr} and P_{sx}, where rolling resistance is reduced with lower normal load. As the torque demand increases, the distribution shifts to close to equal between the axles. With couplings, the single-axle mode is favorable up to a certain threshold where torque is redistributed to both axles. The two-axle drive is close to equal, with slightly more torque distributed to the rear axle.

The effect on energy consumption during moderate driving, however, is not large. Table 4.3 presents the energy consumption with and without tire losses considered in generating the LUT using the brute force method. When tire losses are included, energy consumption improves by 3.9% compared to ED, whereas considering only electric losses results in a 3.6% improvement.

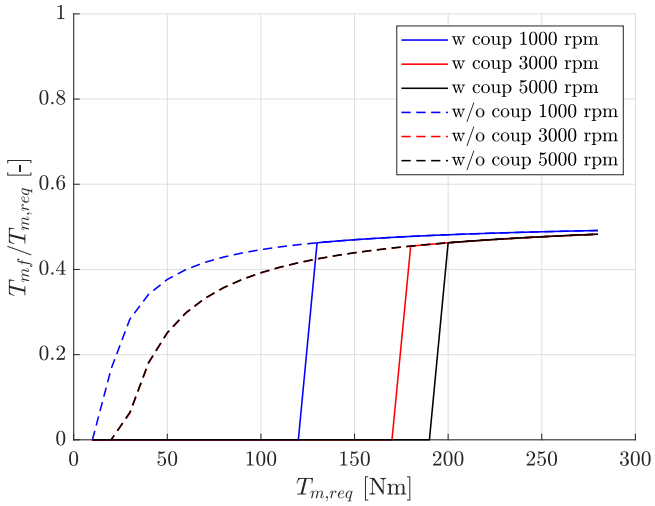

Figure 4.7: *Optimal front to total torque distribution with and without couplings considering only electric losses for three different motor speeds.*

Consequently, incorporating tire power losses into the optimization yields an additional 0.3% reduction in energy consumption. However, as previously declared, this analysis is based on moderate driving conditions. A more aggressive driving style leads to higher longitudinal slip values, which, in turn, result in higher longitudinal slip losses. Therefore, the impact of including tire losses in the optimization of torque distribution could be more significant under such conditions.

Table 4.3: *Energy consumption GCC: the effect of longitudinal tire power losses.*

Strategy	E_{cons} [Wh/km]	ΔE_{cons}
ED	184.4	ref
LUT w. coupling	177.2	-3.9%
LUT w. coupling only el. loss	177.8	-3.6%

4.4.2 Left-to-right torque distribution: lateral tire slip losses

The lateral tire slip losses contribute significantly to the total power consumption (excluding drivetrain losses) during mild cornering, accounting for approximately 17% (Paper C). As outlined in Section 2.2.2, the lateral tire slip losses can be affected by a direct yaw moment.

The power-optimal direct yaw moment

The power-optimal direct yaw moment, M^*_{dir}, minimizing lateral power losses is found by formulating an optimization problem in the form of a QP using a single-track linear vehicle model during steady state cornering. The objective function consists of a quadratic expression of lateral slip power loss, to be minimized by finding the optimal lateral forces and direct yaw moment (the optimization variables), such that vehicle lateral and yaw motion is fulfilled. The power-optimal direct yaw moment, according to Paper C, results in,

$$M^*_{dir} = \frac{C_{y,f} l_r - C_{y,r} l_r}{C_{y,f} + C_{y,r}} m a_y \tag{4.5}$$

The consequent optimal slip angles,

$$\alpha_f^* = \alpha_r^* = -\frac{1}{C_{y,f} + C_{y,r}} m a_y \tag{4.6}$$

Equal slip angles on the front and rear axle implies neutral steering, which results in a destabilizing yaw moment ($M_{dir}^* > 0$) for understeered vehicles, and a stabilizing yaw moment ($M_{dir}^* < 0$) for oversteered vehicles. Similar results are found in [32], where under- and oversteer was induced by accelerating and braking in a curve, respectively.

M_{dir^*} is validated using a high-fidelity vehicle model in IPG CarMaker where it is realized by equally distributing the torque between the front and rear motors on each side. To investigate the dependence on understeer gradient, the balance between front and rear lateral tire stiffnesses are modified. Figure 4.8 presents the lateral slip power loss and slip angles for a range of direct yaw moments in an understeered and oversteered version of the same vehicle.

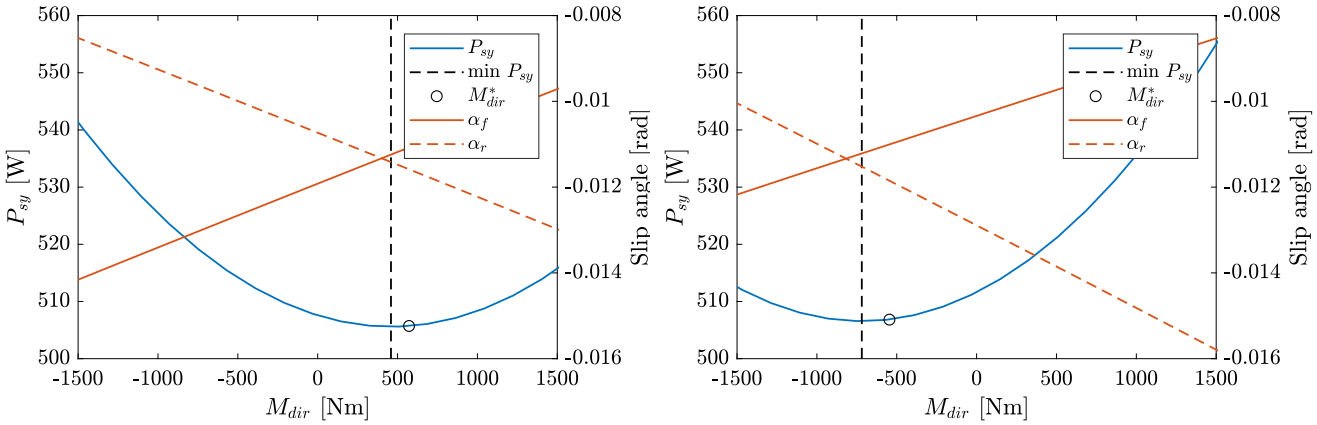

(a) *Understeered case:* $K_{us} = 0.0009$.

(b) *Oversteered case:* $K_{us} = -0.0009$.

Figure 4.8: *Dependency of lateral tire slip loss and tire slip angles on direct yaw moment for two understeer gradients.*

As can be observed, the optimal direct yaw moment coincides well with the slip angles being equal and minimum lateral tire slip losses. The resulting reduction in losses compared to not applying any direct yaw moment is reported in Table 4.4. The results indicate that a higher

Table 4.4: *Lateral tire slip loss at M_{dir}^* for different understeer gradients.*

K_{us}	M_{dir}^* [Nm]	P_{sy} [W]	ΔP_{sy} to $M_{dir} = 0$
-0.0018	-1047	507.0	-2.9 %
-0.009	-551	506.8	-0.9%
0.009	555	505.7	-0.4%
0.0018	1097	508.5	-1.8%

degree of understeer or oversteer corresponds to a greater potential for reducing lateral tire slip losses. This outcome is expected, as minimizing losses requires equal slip angles, and the level of understeer or oversteer increases with the difference between slip angles.

Generation of the power-optimal direct yaw moment

Although Table 4.4 presents promising results, the reduction in lateral slip losses does not directly translate to a decrease in the vehicle's total power consumption. This is due to two factors: (1) longitudinal tire slip losses that inherently result from generating the direct yaw moment through torque vectoring, and (2) the relatively small magnitude of the reduction in lateral power losses compared to the total power consumption.

To include the effects on longitudinal tire slip losses, a power-optimal direct yaw moment for the combined tire slip losses, $M^*_{dir,tot}$, is found through simulation. The results, reported in Table 4.5, indicate that $M^*_{dir,tot}$ reduces significantly compared to M^*_{dir}, and marginal reductions in total power consumption P_b are observed, ranging from 0.03% to 0.16%. Furthermore, this analysis excludes power losses in the motors, which increase due to the generation of the optimal yaw moment, as optimal motor operation for the considered powertrain configuration favors equal torque distribution (as shown in Figure 4.7).

Table 4.5: *Total tire slip loss at $M^*_{dir,tot}$ for different understeer gradients.*

K_{us}	$M^*_{dir,tot}$ [Nm]	$P_{sy} + P_{sx}$ [W]	$\Delta(P_{sy} + P_{sx})$ to $M_{dir} = 0$	ΔP_b to $M_{dir} = 0$
-0.0018	-448	516.1	-1.03%	-0.13 %
-0.009	-244	509.3	-0.3%	-0.03%
0.009	194	505.9	-0.19%	-0.04%
0.0018	392	513.2	-0.77%	-0.16%

Accelerating and decelerating during cornering has not been considered here. These situations increase both longitudinal and lateral tire slip losses as the propulsive forces are increased, and the level of under- and oversteer increased due to longitudinal load transfer, potentially leading to greater savings in tire slip loss through direct yaw moment.

Based on the results found in this work and literature, the following conclusions can be made: (i) to minimize lateral tire slip losses, understeer characteristics resembling neutral-steer should be employed, resulting in destabilizing and stabilizing direct yaw moments for understeered and oversteered vehicles, respectively, (ii) how much one can affect lateral tire slip losses depend on lateral acceleration, where the impact is greater at larger lateral accelerations [15] (iii) during moderate driving, the energy-optimal understeer characteristic is dependent on powertrain efficiency [24], as the impact of tire slip loss on energy consumption is minor.

4.5 Key findings

To summarize this chapter, the following key findings are identified:

- Considering a powertrain configuration with identical PMSMs, the ability to mechanically couple/decouple is the main contributor to power loss minimization.
- Joint optimization of torque distribution and transmission ratios result in significant energy savings, compared to optimizing the ratios using a fixed torque distribution.
- During moderate driving, the impact of torque distribution on minimizing both longitudinal and lateral tire slip power losses is limited. Although the power loss due to rolling resistance is large, its dependence on applied torque is small.

5

Concluding remarks

This thesis explores different approaches to reducing the energy consumption, related to vehicle motion and actuator selection, of overactuated battery electric vehicles by means of predictive and instantaneous optimization methods. Everyday driving is considered to target the area in which improvements in energy consumption will have the largest effect on a global scale. The following section addresses the identified research questions based on the findings presented in the preceding chapters.

RQ1. What are the energy consequences of a hierarchical functional decomposition, i.e., separating the optimization of longitudinal velocity trajectory and torque distribution, in overactuated battery electric vehicles?

A hierarchical decomposition is realized by a de-centralized optimization architecture, in which the optimization of velocity trajectory and torque distribution is separated into a predictive and instantaneous optimization problem, respectively. The de-centralized architecture is compared to a centralized optimization architecture, in which the optimization of velocity trajectory and torque distribution is performed jointly in a predictive optimization framework. The hierarchical decomposition results in higher energy consumption, most prominent in low velocity scenarios. The energy consumption is increased by 3.5% at low velocities, and 0.1% at high velocities. Considering the Artemis urban drive cycle, the energy consumption is increased by 2.2%. The dependence on velocity can be explained by the characteristics of the efficiency maps of the electric motors, where the variation in efficiency is mainly dependent on velocity in the low velocity region. As a result, the velocity trajectories in low velocity scenarios vary significantly between the centralized and de-centralized architecture. Consequently, the energy consumption is affected.

RQ2. How can the optimization of the velocity trajectory be augmented with information about the combined powertrain efficiency, without increasing the number of optimization variables, to mitigate the energy consequences associated with decoupling velocity planning from torque distribution?

The energy consequences of the de-centralized architecture are minimized by augmenting the objective function of the predictive problem formulation with information on the combined powertrain efficiency, resulting in the refined de-centralized architecture. The information is provided as an aggregated power loss map, which is generated using the optimal motor torque

distribution and defined as a function of vehicle longitudinal force and velocity. With the aggregated power loss map, the energy consequences are reduced, leading to a 0.4% increase in energy consumption at low velocities, and 0% at high velocities and in the Artemis urban cycle, compared to the centralized architecture.

RQ3. How to coordinate actuators, i.e., allocate individual motor torques and determine coupling/decoupling of motors, to minimize power losses and at the same time follow the driver's intention on vehicle motion?

Optimization-based control allocation is employed to distribute torque optimally while meeting the vehicle motion demands. The two methods explored in this thesis, a lookup table generated using a brute force approach and an analytically solved quadratic programming algorithm, each contribute to a 3.9% reduction in energy consumption compared to equal torque distribution. In a powertrain consisting of identical permanent magnet synchronous motors, any attempt to minimize energy consumption through optimal torque distribution, without enabling motor decoupling from the wheels, is largely ineffective due to the significant power losses associated with motor rotation. Considering identical motors, the single-axle drive is power-optimal for low total torque demands, while equal distribution between the axles is power-optimal for high total torque demands.

The effectiveness of algorithms designed to minimize power losses inevitably depends on which losses are considered. As previously stated, couplings play a critical role in unlocking the full potential for reducing motor-generated power losses. Additionally, tire losses arise in the conversion of wheel torque to wheel force, and these can be partially mitigated through deliberate torque distribution. However, under moderate driving conditions, tire losses are relatively small compared to motor losses. Including longitudinal tire losses in the power loss objective function, in addition to motor losses, yields an additional 0.3% reduction in energy consumption compared to excluding them. While lateral tire slip losses become significant during steady-state cornering, they are not substantially influenced by torque vectoring at moderate lateral accelerations.

RQ4. How do different transmission ratios, when combined with power-optimal torque distribution, affect the potential for minimizing energy consumption in battery electric vehicles?

The energy-optimal transmission ratios for the front and rear motors are identified for an everyday drive cycle using the brute-force method. These ratios depend on the torque distribution strategy: equal wheel torque distribution results in identical ratios on both axles, whereas power-optimal torque distribution using a control allocator yields a higher ratio on the front axle and a lower ratio on the rear. This setup resembles the startability and cruise axle concept, where one axle is optimized for low-speed and the other for high-speed efficiency. The resulting energy savings amount to 8.4% compared to the optimal ratio combination based on equal wheel torque distribution. The location of the higher and lower ratio, i.e., front or rear axle, is determined by tire power losses.

6

Future work

The findings of this thesis open up several interesting directions for future research. The most relevant ones are discussed in this section.

Experimental validation and implementation
The most important direction for future work is experimental validation. As the results in this thesis are based on simulation, the proposed control allocation algorithms and function architecture concepts should be verified by on-road testing. The driving conditions and vehicle parameters are assumed to be known, e.g., tire stiffness, tire radius, road inclination, no headwind, etc., but are in reality estimated and subject to error. A sensitivity analysis should be made on estimated parameters and variables to assess their influence on the optimal torque distribution and energy consumption. Furthermore, the optimality of the energy-optimal velocity trajectory can only be ensured if real-world conditions perfectly match those modeled in the predictive layer. A simplified model is used which, in addition to estimated vehicle parameters and driving conditions, contribute with errors. However, although using a high-fidelity vehicle model in the predictive layer potentially leads to more optimal solutions in simulation, it might not increase optimality in reality as it requires detailed knowledge of parameters and variables which are subject to estimation errors. To assess the required level of model complexity, one could start with a particle model and stepwise increase the complexity until the accuracy of the prediction deteriorates.

Integration with existing vehicle stability systems
Redistribution of wheel torque between axles, particularly during cornering, can lead to vehicle instability. For example, during moderate driving, unstable situations may occur due to low tire-road friction. Under such driving conditions, excessive torque distributed to the rear axle could potentially lead to high rear side slip, leading to loss of control. Although it is assumed that existing vehicle stability systems, such as ABS, TC and electronic stability control (ESC), have priority and intervene if unsafe situations occur, an abrupt switch between the systems could lead to occupant discomfort and dissatisfaction, potentially turning off the energy-efficient system. Therefore, the integration of torque distribution algorithms with existing motion control functions in the vehicle requires consideration in the future.

Extending the EMP with lateral motion planning
Including only the longitudinal motion in the motion planning layer may lead to excessive velocities during cornering, causing occupant discomfort and possibly instability due to too high lateral accelerations. This risk is higher for rural roads, which in general have more dynamic and greater curvatures than highways. To include lateral motion, the objective function can be augmented to incorporate occupant comfort and/or stability in terms of, e.g., lateral acceleration

and jerk. In this way, the trade-off between energy and comfort/stability can be tuned by using different weightings of the terms in the objective function.

Computational efficiency of the decoupled EMP
Although the algorithms in this work are not optimized for computational efficiency, a significant difference in computation time was seen for Artemis urban drive cycle where DCA and r-DCA were more than twice as fast as CA (CA: 22.875 s, DCA: 2.267 s, r-DCA: 8.667 s on a standard laptop computer with an Intel i7 3.00 GHz processor). To properly analyze the computational effort, the algorithms should be optimized for convergence, and then compared. Furthermore, it is difficult to secure a safety case if algorithms are not converging. This is a concern which also, besides computational efficiency, limits how advanced the algorithms can be in road vehicles for public roads.

Cost related to coupling events
If there is a cost related to the couple/decouple event, the number of events over time requires consideration, transforming it into a dynamic optimization problem. In [61] for example, the coupling/decoupling event is penalized in a MPC framework with a 5 s horizon. It is shown that the number of coupling/decoupling events can be reduced by approximately 80% with minor influence on the energy consumption. Similar results are found by [62]. Although the APLM will provide the power-optimal coupled/decoupled motor combinations, it does not capture the actual event-related cost. In this case, the task of separating the optimization of velocity trajectory and torque distribution will be more complex. Thus, other methods to convey powertrain information to the predictive layer in the de-centralized architecture, and how to integrate coupling/decoupling decisions when it is associated with a cost, should be explored in the future. Furthermore, the coupling management strategy should take drivetrain oscillations into consideration as they can affect occupant comfort negatively.

Appendices

A

Derivation of battery power losses

The battery can be modeled as an equivalent electric circuit with an ideal voltage source and an ohmic resistance connected in series, presented in Figure A.1, where V_{b0} represents an ideal voltage source and R_b battery internal resistance. The derivation of the power supplied to or

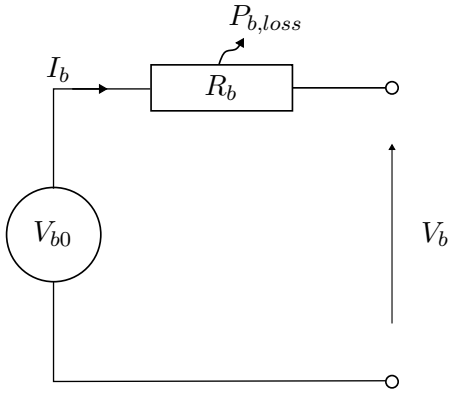

Figure A.1: *Equivalent circuit of a battery.*

drawn from the battery, P_b, follows,

$$P_b = I_b V_{b0} \tag{A.1}$$
$$P_m = I_b V_b \tag{A.2}$$
$$P_{b,loss} = I_b^2 R_b \tag{A.3}$$
$$P_b = P_{b,loss} + P_m \tag{A.4}$$

where P_m is electric power supplied to or generated by the motor. Combining (A.1)-(A.4) yields,

$$P_{b,loss} = \left(\frac{P_m + P_{b,loss}}{V_{b0}} \right)^2 R_b \tag{A.5}$$

Rearranging (A.5),

$$0 = P_{b,loss}^2 + \left(2P_m - \frac{V_{b0}^2}{R_b} \right) P_{b,loss} + P_m^2 \tag{A.6}$$

Solving for $P_{b,loss}$,

$$P_{b,loss} = -P_m + \frac{V_{b0}^2}{2R_b} \pm \sqrt{V_{b0}^2 \left(\frac{V_{b0}^2 - 4P_m R_b}{4R_b^2} \right)} \tag{A.7}$$

Combining (A.4) and (A.7), with the assumption that when $P_m = 0$, then $P_b = 0$, only one solution remains and the expression for P_b is found,

$$P_b = \frac{V_{b0}^2}{2R_b} - V_{b0}\sqrt{\frac{V_{b0}^2 - 4P_m R_b}{4R_b^2}} \tag{A.8}$$

A simple analysis can be made to compare the battery losses to the losses in the electric motors. When referring to the losses in the electric motors here, the losses in the inverters are included. A modern lithium-ion battery has an internal resistance $R_b = 0.11\ \Omega$ of the complete battery pack and an ideal voltage $V_{b0} = 800\ V$. It is assumed that the battery is ideally conditioned, meaning that it operates at an optimal temperature and that the SOC stays within limits such that the internal resistance can be considered constant. By using the power demand from two scenarios used in this thesis (Paper D), a comparison of the power losses is presented in Figure A.2. The magnitude of the battery losses in relation to the motor losses depends on velocity.

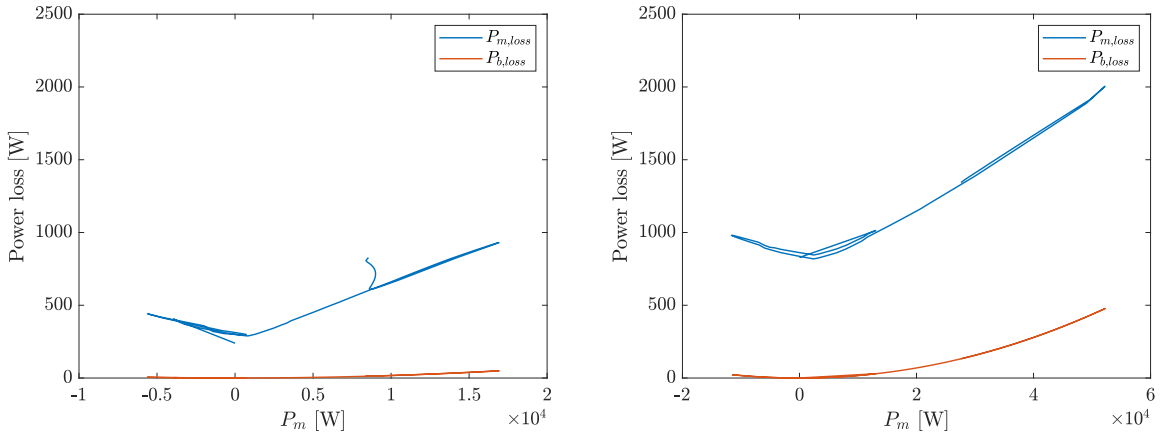

(a) *15 km/h* **(b)** *90 km/h*

Figure A.2: *Comparison of power losses between battery and two electric motor pairs (from Paper D).*

During low speed, presented in Figure A.2a, the battery losses are 20 times smaller than the motor losses. It can therefore be assumed that the battery losses are negligible in this situation. During high speed, presented in Figure A.2b, this assumption leads to greater estimation errors as the battery losses in this situation are approximately 4 times smaller than the motors losses. However, the battery and motor share a quadratic relationship with motor power demand, P_m, with the minimum in approximately the same position. Therefore, solutions that minimize the losses in the motors will also minimize the losses in the battery. It is assumed that including the battery losses in the optimization will change the final value on energy consumption which is essential for range estimation, but not the optimal velocity profiles provided the conditions stated earlier. Therefore, it can be neglected in the conceptual study performed in this work.

B

Derivation of power loss at the wheels

The mechanical power of the wheels can be expressed as a sum of the products of wheel torque T_i and wheel rotational speed ω_i for tire $i \in [1, 4]$.

$$P_{w,tot} = \sum_{i=1}^{4} P_{w,i} = \sum_{i=1}^{4} T_i \omega_i \tag{B.1}$$

Neglecting the effect of wheel dynamics, i.e. $J_w \dot{\omega}_i = 0$, the wheel torque and rotational speed can be expressed as

$$T_i = r_l F_{x,i} + C_{rr} F_{z,i} \tag{B.2}$$

$$\omega_i = (1 + \kappa_i) \frac{v_{xw,i}}{r_e} \tag{B.3}$$

where r_l represents the loaded tire radius, r_e the effective tire radius ($r_e = v_x/\omega$ of the freely rolling tire), C_{rr} the rolling resistance coefficient, $F_{z,i}$ the normal load of tire i, $F_{x,i}$ the longitudinal force, κ_i the longitudinal tire slip and $v_{xw,i}$ the longitudinal velocity of the wheel hub in the wheel coordinate system,

$$v_{xw,i} = v_{x,i} \cos\delta + v_{y,i} \sin\delta \tag{B.4}$$

where $v_{x,i}$ and $v_{y,i}$ are the longitudinal and lateral wheel corner velocities in the vehicle coordinate system. A large path radius is assumed, thereby assuming small angles $\left(\cos\delta \approx 1, \sin\delta \approx \delta, \delta^2 \approx 0\right)$, $v_x >> v_y\delta$ and $\frac{w}{2} >> l_f\delta$, the longitudinal wheel velocity $v_{xw,i}$ is approximated to $v_{x,i}$ where

$$v_{x,i} = v_x - \frac{w}{2}\omega_z \quad \text{for i = 1,3} \tag{B.5}$$

$$v_{x,i} = v_x + \frac{w}{2}\omega_z \quad \text{for i = 2,4} \tag{B.6}$$

The equations of motion for a front wheel steered two-track vehicle model are formulated accordingly,

$$m(\dot{v}_x - v_y\omega_z) = (F_{x,1} + F_{x,2})\cos\delta_f + F_{x,3} + F_{x,4} - (F_{y,1} + F_{y,2})\sin\delta_f - F_{air} - F_g \tag{B.7}$$

$$m(\dot{v}_y + v_x\omega_z) = (F_{y,1} + F_{y,2})\cos\delta_f + F_{y,3} + F_{y,4} + (F_{x,1} + F_{x,2})\sin\delta_f \tag{B.8}$$

$$I_{zz}\dot{\omega}_z = (F_{y,1} + F_{y,2})\cos\delta_f l_f - (F_{y,3} + F_{y,4})\, l_r + (F_{x,1} + F_{x,2})\sin\delta_f l_f + M_{dir} + \frac{w}{2}(F_{y,1} - F_{y,2})\sin\delta_f \tag{B.9}$$

where m is the vehicle mass, v_x is the longitudinal velocity at center of gravity, v_y the lateral velocity at center of gravity, ω_z is the yaw rate, I_{zz} is the yaw inertia, $F_{x,i}$ is longitudinal force for tire i, $F_{y,i}$ is the lateral tire force, $F_{air} = 0.5 A_f C_d \rho_{air} v_x^2$ is the aerodynamic drag and

$F_g = mg\sin\phi$ is the grade resistance, ϕ is the slope angle, δ_f is the front wheel angle and M_{dir} is the direct yaw moment defined as

$$M_{dir} = \frac{w}{2}\left(-F_{x,1} + F_{x,2} - F_{x,3} + F_{x,4}\right) \tag{B.10}$$

Combined tire slip is neglected in the sense that the influence of longitudinal and lateral tire slip on lateral and longitudinal force respectively, is neglected. Assuming the same slip angle between the tires on the front and rear axle,

$$\alpha_f = \beta + \frac{l_f\omega_z}{v_x} - \delta_f \qquad \alpha_r = \beta - \frac{l_r\omega_z}{v_x} \tag{B.11}$$

Using a linear tire model,

$$F_{y,i} = -C_{yw,i}\alpha_i \tag{B.12}$$

Where $C_{yw,i}$ is the lateral tire stiffness of tire i. Assuming that the lateral tire stiffness increases or decreases proportional to the lateral load transfer.

$$C_{yw,i} = CC_{y,j}\left(F_{z0,j} - \Delta F_{z,j}\right) \quad \text{for } i \in [1,3] \tag{B.13}$$
$$C_{yw,i} = CC_{y,j}\left(F_{z0,j} + \Delta F_{z,j}\right) \quad \text{for } i \in [2,4] \tag{B.14}$$

where $CC_{y,j}$ is a proportionality constant, $F_{z0,j}$ is the static normal load and $\Delta F_{z,j}$ the change in normal load due to lateral load transfer on axle j. Disregarding load transfer, the front and rear lateral forces can then be expressed as,

$$F_{y,j} = -2CC_{y,j}F_{z0,j}\alpha_j = -C_{y,j}\alpha_j \tag{B.15}$$

where $C_{y,j} = 2CC_{y,j}F_{z0,j}$.

Finally, an expression for the required input power to the wheels from the wheel torque actuators can be found by combining (B.1)-(B.15), assuming $r_l \approx r_e$.

$$\begin{aligned} P_{w,tot} = \; & \underbrace{mv_x\dot{v}_x + mv_y\dot{v}_y + I_{zz}\omega_z\dot{\omega}_z}_{\text{inertial resistance, } P_{inert}} + \underbrace{F_{air}v_x + F_g v_x}_{\text{motion resistance, } P_{res}} + \underbrace{\sum_{i=1}^{4} C_{rr}F_{z,i}\omega_i}_{\text{rolling resistance, } P_{rr}} \\ & - \underbrace{v_x\left(F_{y,f}\alpha_f + F_{y,r}\alpha_r\right)}_{\text{cornering resistance, } P_{cr}} + \underbrace{\sum_{i=1}^{4} F_{x,i}\kappa_i v_{x,i}}_{\text{longitudinal slip loss, } P_{sx}} - \delta_f(v_y + \omega_z l_f)(F_{x,1} + F_{x,2}) \end{aligned} \tag{B.16}$$

The last term consists of the component of the tire longitudinal force that is aligned with the lateral direction. This effect is not considered in this thesis.

C

Derivation of the analytical solution to QP

The analytical solution to the quadratic program is derived using the Karush-Kuhn-Tucker (KKT) conditions for optimality. The KKT conditions are necessary conditions for a solution to be optimal in a constrained optimization problem. For convex problems, they are sufficient for global optimality [63].

Consider problem (2.19) with no inequality constraints,

$$\min_{\boldsymbol{x}\in\mathbb{R}^n} \quad f(\boldsymbol{x}) \tag{C.1}$$

$$\text{such that} \quad h(\boldsymbol{x}) = 0_m \tag{C.2}$$

The KKT conditions for this problem state that at a local minimum $\boldsymbol{x}^*$ of f over a feasible set, there exists a vector $\boldsymbol{\lambda}^* \in \mathbb{R}^m$ such that,

$$\nabla_{\boldsymbol{x}}\mathcal{L}(\boldsymbol{x}^*, \boldsymbol{\lambda}^*) := \nabla f(\boldsymbol{x}^*) + \sum_{j=1}^{m} \lambda_j^* \nabla h_j(\boldsymbol{x}^*) = \mathbf{0}^n \tag{C.3}$$

$$\nabla_{\boldsymbol{\lambda}}\mathcal{L}(\boldsymbol{x}^*, \boldsymbol{\lambda}^*) := \boldsymbol{h}(\boldsymbol{x}^*) = \mathbf{0}^m \tag{C.4}$$

where $\boldsymbol{\lambda}$ denotes the Lagrangian multipliers and $\mathcal{L}$ the Lagrangian function defined as,

$$\mathcal{L}(\boldsymbol{x}, \boldsymbol{\lambda}) = f(\boldsymbol{x}) + \sum_{j=1}^{m} \lambda_j h_j(\boldsymbol{x}) \tag{C.5}$$

Accordingly, the Lagrangian function of the QP is given by,

$$\mathcal{L}(\boldsymbol{u}, \boldsymbol{\lambda}) = \frac{1}{2}\boldsymbol{u}^T Q \boldsymbol{u} + f^T \boldsymbol{u} + \boldsymbol{\lambda}^T (B\boldsymbol{u} - \boldsymbol{v}) \tag{C.6}$$

with partial derivatives according to,

$$\begin{bmatrix} \nabla\mathcal{L}_{\boldsymbol{u}} \\ \nabla\mathcal{L}_{\boldsymbol{\lambda}} \end{bmatrix} = \begin{bmatrix} Q & B^T \\ B & \mathbf{0} \end{bmatrix} \begin{bmatrix} \boldsymbol{u} \\ \boldsymbol{\lambda} \end{bmatrix} + \begin{bmatrix} f \\ -\boldsymbol{v} \end{bmatrix} \tag{C.7}$$

Applying the KKT conditions (C.3) and (C.4), the analytical solution is found by,

$$\begin{bmatrix} \boldsymbol{u}^* \\ \boldsymbol{\lambda}^* \end{bmatrix} = \begin{bmatrix} Q & B^T \\ B & \mathbf{0} \end{bmatrix}^{-1} \begin{bmatrix} -f \\ \boldsymbol{v} \end{bmatrix} \tag{C.8}$$

References

[1] Agency, E. E. "Transport and environment report 2022 - Digitalisation in the mobility system: challenges and opportunities". DOI: 10.2800/47438. URL: http://europa.eu.

[2] Agency, E. E. "New registrations of electric vehicles in Europe". 2024. URL: https://www.eea.europa.eu/en/analysis/indicators/new-registrations-of-electric-vehicles?activeAccordion= (visited on 2025-02-06).

[3] Wicki, M. et al. "What do we really know about the acceptance of battery electric vehicles?–Turns out, not much". *Transport Reviews* **43** (1 2023), 62–87. ISSN: 14645327. DOI: 10.1080/01441647.2021.2023693.

[4] Bingham, C., Walsh, C., and Carroll, S. "Impact of driving characteristics on electric vehicle energy consumption and range". *IET Intelligent Transport Systems* **6** (1 2012-03), 29–35. ISSN: 1751956X. DOI: 10.1049/iet-its.2010.0137.

[5] Jafari, M. et al. "Simulation and Analysis of the Effect of Real-World Driving Styles in an EV Battery Performance and Aging". *IEEE Transactions on Transportation Electrification* **1**.4 (2015), 391–401. DOI: 10.1109/TTE.2015.2483591.

[6] Arrowhead, M.-B. of. "How To Use the ECO Assist Feature in the Latest Mercedes-Benz EQB?" 2025. URL: https://www.arrowheadmb.com/blog/how-to-use-the-eco-assist-feature-in-the-latest-mercedes-benz-eqb/ (visited on 2025-04-15).

[7] Trucks, V. "I-See". URL: https://www.volvotrucks.co.uk/en-gb/trucks/features/i-see.html (visited on 2024-02-02).

[8] Scania. "Updated CCAP from Scania can save up to 2% fuel". 2023. URL: https://www.scania.com/group/en/home/newsroom/press-releases/press-release-detail-page.html/4538481-updated-ccap-from-scania-can-save-up-to-2--fuel# (visited on 2024-02-15).

[9] Härkegård, O. "Backstepping and control allocation with applications to flight control". PhD thesis. Linköping University, 2003.

[10] Johansen, T. A. and Fossen, T. I. "Control allocation - A survey". *Automatica* **49** (5 2013), 1087–1103. ISSN: 00051098. DOI: 10.1016/j.automatica.2013.01.035.

[11] Chen, Y. and Wang, J. "Energy-efficient control allocation for over-actuated systems with electric vehicle applications". *ASME 2010 Dynamic Systems and Control Conference, DSCC2010* **1** (2010), 37–44. DOI: 10.1115/DSCC2010-4012.

[12] Gu, J. et al. "Energy efficiency optimization of electric vehicle driven by in-wheel motors". *International Journal of Automotive Technology* **14** (5 2013), 763–772. DOI: 10.1007/s1223901300841.

[13] Song, Z. et al. "Torque Distribution Strategy for Multi-PMSM Applications and Optimal Acceleration Control for Four-Wheel-Drive Electric Vehicles". *Journal of Dynamic Systems, Measurement and Control, Transactions of the ASME* **142** (2 2020-02). ISSN: 15289028. DOI: 10.1115/1.4045321.

[14] Yuan, X. and Wang, J. "Torque distribution strategy for a front- and rear-wheel-driven electric vehicle". *IEEE Transactions on Vehicular Technology* **61** (8 2012), 3365–3374. ISSN: 00189545. DOI: 10.1109/TVT.2012.2213282.

[15] Filippis, G. D. et al. "Energy-Efficient Torque-Vectoring Control of Electric Vehicles with Multiple Drivetrains". *IEEE Transactions on Vehicular Technology* **67** (6 2018), 4702–4715. ISSN: 00189545. DOI: 10.1109/TVT.2018.2808186.

[16] Pennycott, A. et al. "Reducing the motor power losses of a four-wheel drive, fully electric vehicle via wheel torque allocation". *Proceedings of the Institution of Mechanical Engineers, Part D: Journal of Automobile Engineering* **228** (7 2014), 830–839. ISSN: 09544070. DOI: 10.1177/0954407013516106.

[17] Fujimoto, H. and Harada, S. "Model-Based Range Extension Control System for Electric Vehicles with Front and Rear Driving-Braking Force Distributions". *IEEE Transactions on Industrial Electronics* **62** (5 2015), 3245–3254. ISSN: 02780046. DOI: 10.1109/TIE.2015.2402634.

[18] Novellis, L. D., Sorniotti, A., and Gruber, P. "Driving modes for designing the cornering response of fully electric vehicles with multiple motors". *Mechanical Systems and Signal Processing* **64-65** (2015), 1–15. ISSN: 10961216. DOI: 10.1016/j.ymssp.2015.03.024. URL: http://dx.doi.org/10.1016/j.ymssp.2015.03.024.

[19] Novellis, L. D., Sorniotti, A., and Gruber, P. "Optimal Wheel Torque Distribution for a Four-Wheel-Drive Fully Electric Vehicle". *SAE International Journal of Passenger Cars - Mechanical Systems* **6** (1 2013), 128–136. ISSN: 19464002. DOI: 10.4271/2013-01-0673.

[20] Wu, X. et al. "Torque optimal allocation strategy of all-wheel drive electric vehicle based on difference of efficiency characteristics between axis motors". *Energies* **12** (6 2019). ISSN: 19961073. DOI: 10.3390/en12061122.

[21] Dizqah, A. M. et al. "A Fast and Parametric Torque Distribution Strategy for Four-Wheel-Drive Energy-Efficient Electric Vehicles". *IEEE Transactions on Industrial Electronics* **63** (7 2016), 4367–4376. ISSN: 02780046. DOI: 10.1109/TIE.2016.2540584.

[22] Lenzo, B. et al. "Torque Distribution Strategies for Energy-Efficient Electric Vehicles with Multiple Drivetrains". *Journal of Dynamic Systems, Measurement and Control, Transactions of the ASME* **139** (12 2017), 1–13. ISSN: 15289028. DOI: 10.1115/1.4037003.

[23] Novellis, L. D., Sorniotti, A., and Gruber, P. "Wheel torque distribution criteria for electric vehicles with torque-vectoring differentials". *IEEE Transactions on Vehicular Technology* **63** (4 2014), 1593–1602. ISSN: 00189545. DOI: 10.1109/TVT.2013.2289371.

[24] Chatzikomis, C. et al. "An energy-efficient torque-vectoring algorithm for electric vehicles with multiple motors". *Mechanical Systems and Signal Processing* **128** (2019-08), 655–673. ISSN: 10961216. DOI: 10.1016/j.ymssp.2019.03.012.

[25] Li, G. et al. "Energy-oriented torque allocation strategy design of 4wid electric vehicle using slope information". *SAE Technical Papers* **2019-April** (April 2019), 1–8. ISSN: 01487191. DOI: 10.4271/2019-01-0461.

[26] Zhang, X. and Göhlich, D. "Optimal torque distribution strategy for a four motorized wheels electric vehicle". *28th International Electric Vehicle Symposium and Exhibition 2015, EVS 2015* (2015), 1–9.

[27] Chen, Y. and Wang, J. "Adaptive energy-efficient control allocation for planar motion control of over-actuated electric ground vehicles". *IEEE Transactions on Control Systems Technology* **22** (4 2014), 1362–1373. ISSN: 10636536. DOI: 10.1109/TCST.2013.2287560.

[28] Chen, Y. and Wang, J. "2011 American Control Conference". IEEE, 2011. ISBN: 9781457700811.

[29] Li, B. et al. "An optimal torque distribution control strategy for four-independent wheel drive electric vehicles". *Vehicle System Dynamics* **53** (8 2015), 1172–1189. ISSN: 17445159. DOI: 10.1080/00423114.2015.1028414. URL: https://doi.org/10.1080/00423114.2015.1028414.

[30] Rill, G. "Reducing the cornering resistance by torque vectoring". *Procedia Engineering* **199** (2017), 3284–3289. ISSN: 18777058. DOI: 10.1016/j.proeng.2017.09.393. URL: http://dx.doi.org/10.1016/j.proeng.2017.09.393.

[31] Filippis, G. D. et al. "Energy-Efficient Torque-Vectoring Control of Electric Vehicles with Multiple Drivetrains". *IEEE Transactions on Vehicular Technology* **67** (6 2018), 4702–4715. ISSN: 00189545. DOI: 10.1109/TVT.2018.2808186.

[32] Kobayashi, T. et al. "Efficient direct yaw moment control: tyre slip power loss minimisation for four-independent wheel drive vehicle". *Vehicle System Dynamics* **56** (5 2018), 719–733. ISSN: 17445159. DOI: 10.1080/00423114.2017.1330483. URL: https://doi.org/10.1080/00423114.2017.1330483.

[33] Chien, P. C. and Chen, C. K. "Integrated chassis control and control allocation for all wheel drive electric cars with rear wheel steering". *Electronics (Switzerland)* **10** (22 2021-11). ISSN: 20799292. DOI: 10.3390/electronics10222885.

[34] Zhao, H. et al. "Model predictive control allocation for stability improvement of four-wheel drive electric vehicles in critical driving condition". *IET Control Theory and Applications* **9** (18 2015-12), 2688–2696. ISSN: 17518652. DOI: 10.1049/iet-cta.2015.0437.

[35] Bottiglione, F. et al. "Energy consumption of a battery electric vehicle with infinitely variable transmission". *Energies* **7** (12 2014), 8317–8337. ISSN: 19961073. DOI: 10.3390/EN7128317.

[36] Ruan, J., Walker, P., and Zhang, N. "A comparative study energy consumption and costs of battery electric vehicle transmissions". *Applied Energy* **165** (2016-03), 119–134. ISSN: 0306-2619. DOI: 10.1016/J.APENERGY.2015.12.081.

[37] Pinto, S. D. et al. "On the comparison of 2- And 4-wheel-drive electric vehicle layouts with central motors and single- And 2-speed transmission systems". *Energies* **13** (13 2020). ISSN: 19961073. DOI: 10.3390/en13133328.

[38] Kwon, K., Seo, M., and Min, S. "Efficient multi-objective optimization of gear ratios and motor torque distribution for electric vehicles with two-motor and two-speed powertrain system". *Applied Energy* **259** (2020-02), 114190. ISSN: 0306-2619. DOI: 10.1016/J.APENERGY.2019.114190.

[39] Dib, W. et al. "Optimal energy management for an electric vehicle in eco-driving applications". *Control Engineering Practice* **29** (2014), 299–307. ISSN: 09670661. DOI: 10.1016/j.conengprac.2014.01.005.

[40] Lu, D. et al. "Optimal velocity control for a battery electric vehicle driven by permanent magnet synchronous motors". *Mathematical Problems in Engineering* **2014** (2014). ISSN: 15635147. DOI: 10.1155/2014/193960.

[41] So, K. M. et al. "On the optimal speed profile for electric vehicles". *IEEE Access* **8** (2020), 78504–78518. ISSN: 21693536. DOI: 10.1109/ACCESS.2020.2982930.

[42] Sciarretta, A., Vahidi, A., et al. "Energy-efficient driving of road vehicles". Springer, 2020.

[43] Koch, A. et al. "Eco-driving for different electric powertrain topologies considering motor efficiency". *World Electric Vehicle Journal* **12** (1 2021-03), 1–19. ISSN: 20326653. DOI: 10.3390/WEVJ12010006.

[44] Liu, Y. et al. "Cooperative optimization of velocity planning and energy management for connected plug-in hybrid electric vehicles". *Applied Mathematical Modelling* **95** (2021-07), 715–733. ISSN: 0307904X. DOI: 10.1016/j.apm.2021.02.033.

[45] Zhuang, W. C. et al. "Integrated energy-oriented cruising control of electric vehicle on highway with varying slopes considering battery aging". *Science China Technological Sciences* **63** (1 2020-01), 155–165. ISSN: 18691900. DOI: 10.1007/s11431-019-9559-2.

[46] Xia, D. et al. "Ecological cooperative adaptive cruise control of over-actuated electric vehicles with in-wheel motor in traffic flow". *IET Intelligent Transport Systems* **15** (6 2021-06), 765–780. ISSN: 1751956X. DOI: 10.1049/itr2.12059.

[47] Al-Wreikat, Y., Serrano, C., and Sodré, J. R. "Effects of ambient temperature and trip characteristics on the energy consumption of an electric vehicle". *Energy* **238** (2022-01). ISSN: 03605442. DOI: 10.1016/j.energy.2021.122028.

[48] Han, J. et al. "Safe-and Eco-Driving Control for Connected and Automated Electric Vehicles Using Analytical State-Constrained Optimal Solution". *IEEE Transactions on Intelligent Vehicles* **3** (2 2018-06), 163–172. ISSN: 23798858. DOI: 10.1109/TIV.2018.2804162.

[49] Genikomsakis, K. N. and Mitrentsis, G. "A computationally efficient simulation model for estimating energy consumption of electric vehicles in the context of route planning applications". *Transportation Research Part D: Transport and Environment* **50** (2017-01), 98–118. ISSN: 13619209. DOI: 10.1016/j.trd.2016.10.014.

[50] Wang, J. et al. "Wheel torque distribution optimization of four-wheel independent-drive electric vehicle for energy efficient driving". *Control Engineering Practice* **110** (2021-05). ISSN: 09670661. DOI: 10.1016/j.conengprac.2021.104779.

[51] Chen, Y. et al. "Energy management and driving strategy for in-wheel motor electric ground vehicles with terrain profile preview". *IEEE Transactions on Industrial Informatics* **10** (3 2014), 1938–1947. ISSN: 15513203. DOI: 10.1109/TII.2013.2290067.

[52] Kim, J. "Optimal power distribution of front and rear motors for minimizing energy consumption of 4-wheel-drive electric vehicles". *International Journal of Automotive Technology* **17** (2 2016), 319–326. DOI: 10.1007/s122390160032y.

[53] Pacejka, H. "Tire and Vehicle Dynamics". Elsevier Science & Technology, 2012.

[54] Ydrefors, L. et al. "Rolling resistance and its relation to operating conditions: A literature review". *Proceedings of the Institution of Mechanical Engineers, Part D* **235**.12 (2021), 2931–2948. DOI: 10.1177/09544070211011089. eprint: https://doi.org/10.1177/09544070211011089. URL: https://doi.org/10.1177/09544070211011089.

[55] Schuring, D. J., Bird, K. D., and Martin, J. F. "Power Requirements of Tires and Fuel Economy." *Tire Science and Technology* **2** (4 1974), 261–285. ISSN: 00908657. DOI: 10.2346/1.2167189.

[56] Hadraoui, H. E. et al. "A Multi-Criteria Analysis and Trends of Electric Motors for Electric Vehicles". *World Electric Vehicle Journal* **13** (4 2022-04). ISSN: 20326653. DOI: 10.3390/wevj13040065.

[57] "Motor technology from Model 3 helps Tesla boost Model S range 10%". https://arstechnica.com/cars/2019/04/motor-technology-from-model-3-helps-tesla-boost-model-s-range-10/. Accessed: 2025-05-12.

[58] Tian, Z., Liu, L., and Shi, W. "A pulse-and-glide-driven adaptive cruise control system for electric vehicle". *International Transactions on Electrical Energy Systems* **31** (11 2021-11). ISSN: 20507038. DOI: 10.1002/2050-7038.13054.

[59] Janardhanan, S. et al. "Concept design of electric cruise and startability axles for long haul heavy vehicles to maximise driving range". Institute of Electrical and Electronics Engineers Inc., 2021. ISBN: 9781665405287. DOI: 10.1109/VPPC53923.2021.9699364.

[60] Pavlovic, J., Marotta, A., and Ciuffo, B. "CO2 emissions and energy demands of vehicles tested under the NEDC and the new WLTP type approval test procedures". *Applied Energy* **177** (2016), 661–670. ISSN: 03062619. DOI: 10.1016/j.apenergy.2016.05.110.

[61] Ganesan, A. et al. "Real-Time Mixed-Integer Energy Management Strategy for Multi-Motor Electric Vehicles". Institute of Electrical and Electronics Engineers Inc., 2023. ISBN: 9798350397420. DOI: 10.1109/ITEC55900.2023.10186957.

[62] Škugor, B. et al. "A parameter-optimised rule-based control strategy for front-rear torque vectoring in electric vehicles with multiple motors and disconnect clutches". *Vehicle System*

Dynamics (2024-11), 1–27. ISSN: 0042-3114. DOI: 10.1080/00423114.2024.2430581. URL: https://www.tandfonline.com/doi/full/10.1080/00423114.2024.2430581.

[63] Niclas, A. et al. "An Introduction to Continous Optimization". Studentlitteratur AB, 2018.

[64] Torinsson, J. et al. "Energy reduction by power loss minimisation through wheel torque allocation in electric vehicles: a simulation-based approach". *Vehicle System Dynamics* **60**.5 (2020), 1488–1511. DOI: 10.1080/00423114.2020.1858121.

[65] Torinsson, J. et al. "Joint Optimization of Transmission and a Control Allocator to Minimize Power Losses in Electric Vehicles". *Advances in Dynamics of Vehicles on Roads and Tracks II. IAVSD 2021* (2021). DOI: 10.1007/978-3-031-07305-2_106.

[66] Torinsson, J. et al. "Upper bounds of lateral tire slip loss minimization during daily driving using torque vectoring". *AVEC'22. 15th International Symposium on Advanced Vehicle Control* (2022).

[67] Torinsson, J. et al. "Energy consequences of separating velocity planning and torque distribution in overactuated electric vehicles". *submitted to Transportation Engineering* (2025).